Computer Modeling in Engineering & Sciences

Tech Science Press

Doi:10.32604/cmes.2025.069481

ARTICLE

Improved Meshfree Moving-Kriging Formulation for Free Vibration Analysis of FGM-FGCNTRC Sandwich Shells

Suppakit Eiadtrong[1,2,#], **Tan N. Nguyen**[3,*,#], **Mohamed-Ouejdi Belarbi**[4] and **Nuttawit Wattanasakulpong**[1,2,*]

[1]Department of Mechanical and Robotic Engineering, School of Engineering and Technology, Walailak University, Thasala, Nakhon Si Thammarat, 80160, Thailand
[2]Center of Excellence for Sustainable Disaster Management, Walailak University, Nakhon Si Thammarat, 80160, Thailand
[3]Department of Architectural Engineering, Sejong University, Seoul, 05006, Republic of Korea
[4]Laboratoire de Recherche en Génie Civil, LRGC, Université de Biskra, Biskra, 07000, Algeria

*Corresponding Authors: Tan N. Nguyen. Email: tnnguyen@sejong.ac.kr; Nuttawit Wattanasakulpong. Email: nuttawit.wa@wu.ac.th

#Suppakit Eiadtrong and Tan N. Nguyen are co-first authors and equally contributed to this work

Received: 24 June 2025; Accepted: 25 August 2025; Published: 30 September 2025

ABSTRACT: An improved meshfree moving-Kriging (MK) formulation for free vibration analysis of functionally graded material-functionally graded carbon nanotube-reinforced composite (FGM-FGCNTRC) sandwich shells is first proposed in this article. The proposed sandwich structure consists of skins of FGM layers and an FGCNTRC core. This structure possesses all the advantages of FGM and FGCNTRC, including high electrical or thermal insulating properties, high fatigue resistance, good corrosion resistance, high stiffness, low density, high strength, and high aspect ratios. Such sandwich structures can be used to replace conventional FGM structures. The present formulation has been established by using an improved meshfree MK method and the first-order shear deformation shell theory (FSDT). The effective material characteristics of the FGM-skin layers and the FGCNTRC core were calculated using the rule of mixture. Key parameters and factors such as the thickness-to-radius ratio, the length-to-radius ratio, layer-thickness ratios, CNT distributions, the volume fraction of CNTs, the power-law index, and various boundary conditions were rigorously investigated. A nonlinear CNT distribution that we term FG-nX is first proposed in this work, and many new results of FGM-FGCNTRC sandwich shells have been provided.

KEYWORDS: Moving kriging; meshfree method; sandwich shells; FGM; FGCNTRC

1 Introduction

Many new materials have been found that have contributed to developments in numerous areas of science and engineering. Functionally graded materials (FGMs) are among those proposed, and many studies have been carried out on them. An FGM is a type of composite material created by mixing two distinct material phases, such as ceramic and metal. As a result, an FGM inherits the characteristics of both material components. For example, an FGM can possess important properties, like good strength, good thermal or electrical insulating properties, or high resistance to fatigue or corrosion. Consequently, such materials are now widely used in semiconductor technologies, aerospace engineering, medical applications, nuclear reactors, etc. Numerous studies have therefore been performed to investigate the behaviors of FGM structures such as beams [1], plates [2–4], and shells [5]. Another modern material- carbon nanotubes (CNTs), which are known as "materials for the 21st century" [6], have attracted considerable attention from researchers in many fields because of their notable mechanical, thermal, and electrical characteristics [7,8]. The discovery of CNTs [9] opened a new area of materials science. Practically, CNTs are very suitable for replacing conventional reinforcements like glass fibers, steel, etc., in composite structures. This is the case because CNTs possess outstanding properties such as low density but with high stiffness, strength, and aspect ratio. A typical study of CNT structures can be found in [10]. In this study, free vibration and buckling behaviors of carbon nanotube-reinforced cross-ply laminated composite plates were obtained by using the method of discrete singular convolution and a first-order shear deformation theory. In structural engineering, sandwich structures are constructed using layers of different materials, and the resulting structures fully inherit the characteristics of each constituent material. This is very useful for improving structural performance, and many types of sandwich beams, plates, and shells have therefore been proposed and investigated. In this article, FGMs and functionally graded carbon nanotube-reinforced composite (FGCNTRC) materials were used to create sandwich shells. The proposed sandwich structure consists of skins of FGM layers and an FGCNTRC core. As mentioned above, this structure possesses all the advantages of both the FGM and the FGCNTRC material. In real-world applications, shells are widely used in mechanical, civil, and aerospace engineering. Some notable applications include the roofs of buildings and stadiums, and shells of ships, cars, submarines, airplanes, and spacecrafts. Thus, the analysis and design of FGM-FGCNTRC sandwich shells are necessary and practical. Another type of FG structure-reinforced with functionally graded graphene platelet has attracted great attention due to its outstanding advantages of being lightweight but with a high load-carrying capacity [11]. In these structures, the graphene platelets are used as reinforcements to enhance the structural stiffness. Results for the vibrations of shells reinforced with graphene platelets considering non-linearity and external load can be found in [12,13]. Results for the thermomechanical free-vibration buckling of FG graphene-reinforced doubly-curved sandwich shells can be found in [14]. Additional studies of functionally graded graphene platelet-reinforced structures should be carried out in the future.

Analytical approaches are only appropriate for problems with simple geometries, boundaries, and loads. Due to these limitations, many numerical methods have been developed for structural analyses, such as the finite element method (FEM) [15], meshfree methods [16–19], isogeometric analysis [20–22], the smoothed FEM [23], etc. In addition, many FEM-based software programs have been successfully developed, such as Abaqus, Sap2000, Ansys, etc. Many meshfree methods have also been proposed, such as the element-free Galerkin method [16], the reproducing kernel particle method [24], the meshless local Petrov-Galerkin method [25], etc. Most of the meshfree methods have a similar limitation that their interpolation functions do not satisfy the Kronecker-delta property. Essential boundary conditions, thus, can not be straightforwardly imposed as in the FEM. Accordingly, several correction techniques for boundaries have been proposed and developed, including Lagrange multipliers [26], penalty methods [27], or a combination with the FEM [28]. Interestingly, the moving-Kriging (MK) interpolation function naturally satisfies the Kronecker-delta property. The meshfree MK method was first proposed to solve the one-dimensional steady-state heat conduction problem [29]. Further developments of this method can be found in [30] for one- and two-dimensional elasticity problems, thin plates [31], shells [32], piezoelectric structures [33], and laminated composite structures [34]. As shown in [29], the accuracy of the MK solutions strongly depends on the quality of the MK interpolation, which is affected by the choice of the correlation parameter θ. However, it is very difficult to find an optimal value for θ. Consequently, an improved meshfree MK method was proposed in [35] to ensure that the MK solutions remain stable and accurate. As numerically demonstrated, the MK shape functions and the solutions of the improved meshfree MK method are independent of changes in θ [35]. To date, the development of the improved meshfree MK method has been limited to the analyses of plate structures [35–37]. In this article, the improved meshfree MK method is first developed for the analysis of shell structures.

As mentioned earlier, sandwich structures possess some outstanding advantages, and numerous studies on the behaviors of sandwich shells made from FGM or FGCNTRC materials have been performed. Typical studies include analyses of shells with an FGM core and two isotropic skins [38,39], conical FGM sandwich shells [40], truncated conical FGM sandwich shells reinforced with FGM stiffeners [41], a structure with a soft viscoelastic core and FGM layers [42], cylindrical FGM sandwich shells reinforced by FGM stiffeners [43], cylindrical FGM sandwich shells reinforced using periodic eccentric ring stiffeners [44], shells with FGCNT face sheets and an isotropic core [45], the nonlinear stability of sandwich shells consisting of a porous FGM and CNT-reinforced composite layers [46], thermal vibrations of shells made of a sandwich of CNTRC sheets on both sides of a porous FG core [47], and conical sandwich shells with FG face sheets and a FG porous core [48]. In this article, we propose sandwich shells consisting of a skin of FGM layers and an FGCNTRC core. The improved MK meshfree method was first developed for modeling curved structures like shells. In addition, an improved meshfree MK formulation for free vibration analysis of FGM-FGCNTRC sandwich shells is first proposed. A nonlinear CNT distribution that we term FG-nX is proposed, and many new results of FGM-FGCNTRC sandwich shells are provided. In this paper, we investigate two types of boundaries, which are simply supported and clamped boundaries. In the case that some structures are connected by bolts or complex boundaries, the necessary information can be found in [49]. FGM-FGCNTRC sandwich shells can be used in semiconductor technologies, aerospace engineering, nuclear reactors, airplanes, spacecrafts, etc. Frequencies and vibrational mode shapes of these applications can be accurately predicted via the proposed technique in this study.

2 First-Order Shear Deformation Theory for FGM-FGCNTRC Sandwich Shells

2.1 Functionally Graded Carbon Nanotube-Reinforced Composite Materials

Fig. 1 shows five types of CNT distributions. UD is the uniform distribution. FG-V, FG-O, and FG-X are three types of linear CNT distributions. For the FG-O distribution, CNTs are enriched at the mid-surface. The top surface is CNT-rich in the case of FG-V distribution, and CNTs are enriched near both the top and bottom surfaces in the case of FG-X distribution. In this article, a nonlinear CNT distribution that we term FG-nX is proposed to enhance the stiffness of FGCNTRC structures. Similar to FG-X, FG-nX is CNT-rich near the top and bottom surfaces, but it is nonlinear through the structural thickness. Fig. 2 shows the FG-nX distribution along the thickness. The volume fraction of CNTs V_{CNT} are determined as follows [50]:

$$
\begin{aligned}
&V_{CNT} = V_{CNT}^{*} && \text{(UD)}\\
&V_{CNT}(z) = \left(1 + \frac{2z}{h}\right) V_{CNT}^{*} && \text{(FG-V)}\\
&V_{CNT}(z) = 2\left(1 - \frac{2|z|}{h}\right) V_{CNT}^{*} && \text{(FG-O)}\\
&V_{CNT}(z) = 2\left(\frac{2|z|}{h}\right) V_{CNT}^{*} && \text{(FG-X)}\\
&V_{CNT}(z) = (\pi/2) sin\left(\frac{\pi|z|}{h}\right) V_{CNT}^{*} && \text{(FG-nX)}
\end{aligned}
\tag{1}
$$

where

$$
V_{CNT}^{*} = \frac{w_{CNT}}{w_{CNT} + (\rho^{CNT}/\rho^{m}) - (\rho^{CNT}/\rho^{m}) w_{CNT}} \tag{2}
$$

where ρ^{CNT} is the density of CNTs, ρ^m is the density of the matrix, and the mass fraction of CNTs is w_{CNT}. Notably, these five types of FGCNTRC shells have the same value of w_{CNT}. The effective characteristics of materials reinforced using CNTs are affected by the structure of CNTs [51–54]. These characteristics can be determined by using micro-mechanical models like the Eshelby-Mori-Tanaka method [55,56] or the rule of mixture [57,58]. In this article, the rule of mixture is utilized because of its simplification as

$$E_{11} = \eta_1 V_{CNT} E_{11}^{CNT} + V_m E^m \tag{3}$$

$$\frac{\eta_2}{E_{22}} = \frac{V_{CNT}}{E_{22}^{CNT}} + \frac{V_m}{E^m} \tag{4}$$

$$\frac{\eta_3}{G_{12}} = \frac{V_{CNT}}{G_{12}^{CNT}} + \frac{V_m}{G^m} \tag{5}$$

where the volume fraction of the matrix is V_m. The notations G_{12}^{CNT}, E_{11}^{CNT} and E_{22}^{CNT} are, respectively, the shear and Young's modulii of the CNTs while G^m and E^m are the corresponding characteristics of the matrix. The efficiency parameters η_i $(i = 1, 2, 3)$ are used in the above formulas to take into account the scale-dependent material characteristics. These parameters are determined by matching the effective characteristics of the CNTs calculated using the rule of mixture with those obtained from molecular-dynamics simulations. In particular, the sum of the volume fractions of the CNTs and the matrix is unity. We determined Poisson's ratio, the density, and the thermal-expansion coefficients α_{11} and α_{22} by utilizing the rule of mixture as

$$\nu_{12} = V_{CNT}^{*} \nu_{12}^{CNT} + V_m \nu^m \tag{6}$$

$$\rho = V_{CNT} \rho^{CNT} + V_m \rho^m \tag{7}$$

$$\alpha_{11} = V_{CNT} \alpha_{11}^{CNT} + V_m \alpha^m \tag{8}$$

$$\alpha_{22} = \left(1 + \nu_{12}^{CNT}\right) V_{CNT} \alpha_{22}^{CNT} + \left(1 + \nu^m\right) V_m \alpha^m - \nu_{12} \alpha_{11} \tag{9}$$

where Poisson's ratios are ν^m, and ν_{12}^{CNT} and the thermal-expansion coefficients are α^m, α_{11}^{CNT}, and α_{22}^{CNT}. Notably, ν_{12} is constant along the structural thickness.

2.2 Functionally Graded Materials

An FGM is a composite material that consists of two distinct material phases which are ceramic and metal. Thus, an FGM fully inherits the mechanical characteristics of these two materials. The volume fractions of the material phases are determined as in [2]

$$V_c(z) = \left(\frac{1}{2} + \frac{z}{h}\right)^n; \quad z \in [-h/2,\ h/2]\ ; \quad V_m = 1 - V_c \tag{10}$$

where V_c and V_m are the volume fractions of ceramic and metal, respectively. As we have seen, not only do V_c and V_m continuously change along the thickness, but also they depend on the power-law index n. In this article, the rule of mixture is utilized to determine the effective characteristics of the FGM [2], as follows:

$$P_e = P_c V_c(z) + P_m V_m(z) \tag{11}$$

here, P_e is an effective characteristic which can be Poisson's ratio ν or Young modulus E or the mass density ρ. The quantities P_c and P_m, respectively, represent the mechanical characteristics of the ceramic and metal.

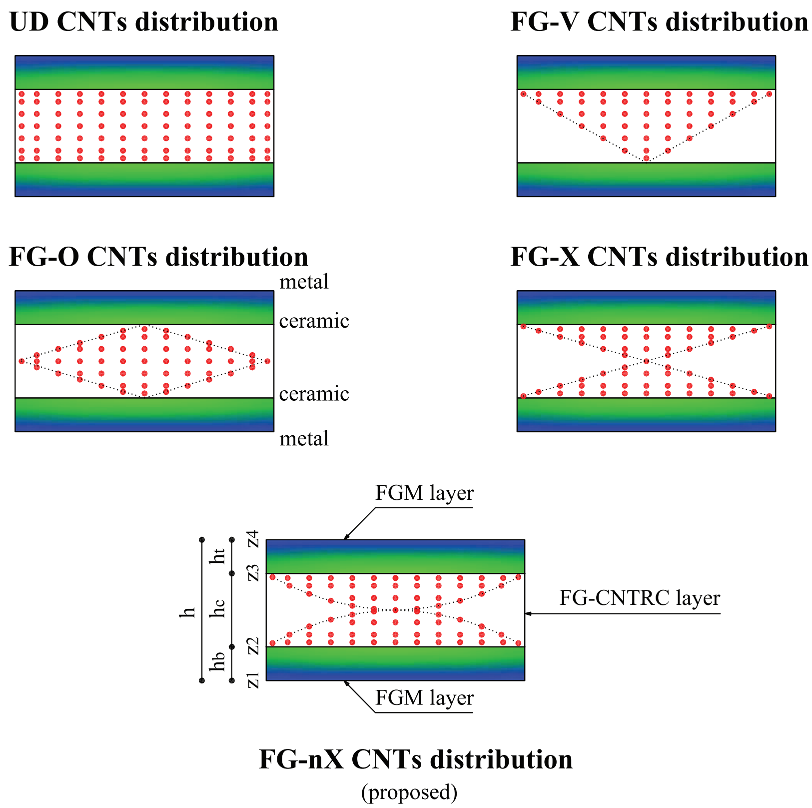

Figure 1: Constitution of an FGM-FGCNTRC sandwich structure

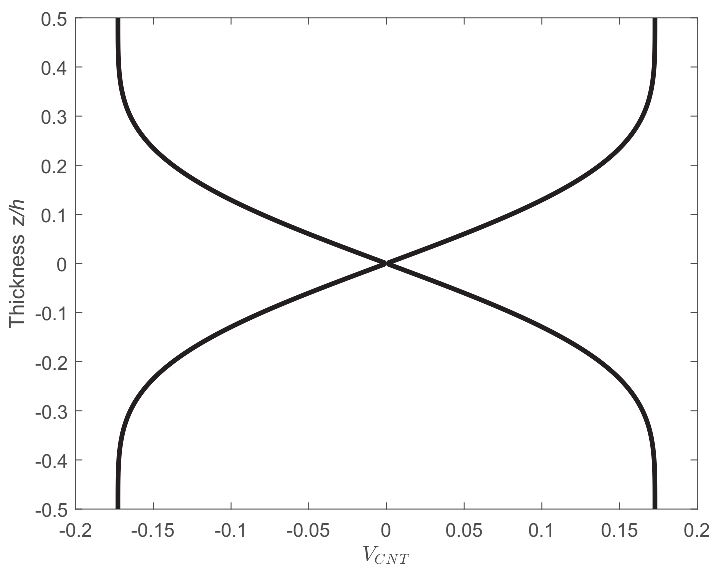

Figure 2: FG-nX distribution (proposed) along the thickness with $V^*_{CNT} = 0.11$

2.3 FGM-FGCNTRC Sandwich Shells

Fig. 1 shows an FGM-FGCNTRC sandwich structure with five types of CNT distributions. It consists of two FGM-skin layers and one FGCNTRC core. For the two FGM-skin layers, the metallic component is enriched at the surfaces $z = z_1$ and $z = z_4$ while the ceramic component is enriched at the surfaces $z = z_2$ and

$z = z_3$. For the FGM skins, the volume fractions of ceramic and metal are determined as follows [3]

$$V_c(z) = \left(\frac{z_4 - z}{z_4 - z_3}\right)^n; z \in \left[z_3, \frac{h}{2}\right], \text{for top skin}$$
$$V_c(z) = \left(\frac{z - z_1}{z_2 - z_1}\right)^n; z \in \left[-\frac{h}{2}, z_2\right], \text{for bottom skin}$$
$$V_m = 1 - V_c \tag{12}$$

where h is the total thickness of the sandwich structure, and $h_b - h_c - h_t$ are the layer-thickness ratios, where h_b, h_c and, h_t, respectively, are the thicknesses of the bottom, core, and top layers. In the case that this ratio is 1-1-1, the thicknesses of the three layers are equal.

2.4 Free Vibration Analysis of FGM-FGCNTRC Sandwich Shells Using First-Order Shear Deformation Shell Theory

We consider a doubly-curved shell with the geometric characteristics shown in Figs. 3 and 4. In these figures, $\mathbf{r}$ denotes the position vector of a point $(x, y, 0)$ on the mid-surface, while $\mathbf{R} = \mathbf{r} + z\hat{\mathbf{n}}$ denotes that of an arbitrary point (x, y, z) within the shell. In addition, ds represents the distance between $(x, y, 0)$ and $(x + \mathrm{d}x, y + \mathrm{d}y, 0)$, computed as follows

$$(\mathrm{d}s)^2 = \mathrm{d}\mathbf{r}.\mathrm{d}\mathbf{r} = a_x^2(\mathrm{d}x)^2 + a_y^2(\mathrm{d}y)^2 \tag{13}$$

and

$$\mathrm{d}\mathbf{r} = \mathbf{g}_x\mathrm{d}x + \mathbf{g}_y\mathrm{d}y; \quad \mathbf{g}_x = \frac{\partial \mathbf{r}}{\partial x}; \quad \mathbf{g}_y = \frac{\partial \mathbf{r}}{\partial y} \tag{14}$$

$\mathbf{g}_x$ and $\mathbf{g}_y$ are, respectively, the tangents to the x- and y-coordinate lines. The surface metrics a_x and a_y are given by

$$a_x^2 = \mathbf{g}_x.\mathbf{g}_x; \quad a_y^2 = \mathbf{g}_y.\mathbf{g}_y \tag{15}$$

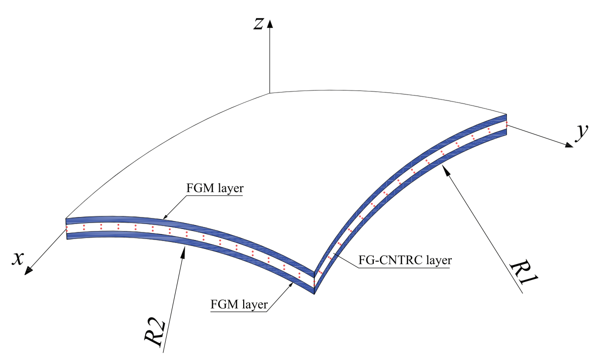

Figure 3: A doubly-curved FGM-FGCNTRC sandwich shell

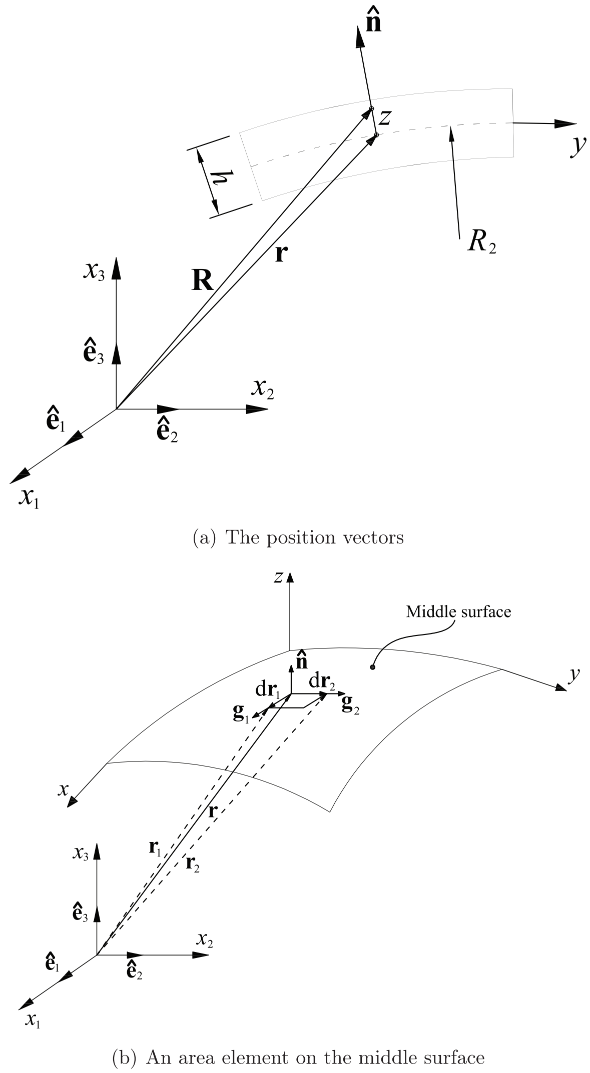

Figure 4: Geometric properties of a doubly-curved FGM-FGCNTRC sandwich shell

The linear strains written in the curvilinear coordinate system are as follows [59,60] for the in-plane strains

$$\varepsilon_{xx} = \frac{1}{A_x}\left(\frac{\partial u}{\partial x} + \frac{1}{a_y}\frac{\partial a_x}{\partial y}v + \frac{a_x}{R_1}w\right)$$
$$\varepsilon_{yy} = \frac{1}{A_y}\left(\frac{\partial v}{\partial y} + \frac{1}{a_x}\frac{\partial a_y}{\partial x}u + \frac{a_y}{R_2}w\right)$$
$$\gamma_{xy} = \frac{A_y}{A_x}\frac{\partial}{\partial x}\left(\frac{v}{A_y}\right) + \frac{A_x}{A_y}\frac{\partial}{\partial y}\left(\frac{u}{A_x}\right) \tag{16}$$

and for the shear strains

$$\gamma_{xz} = \frac{1}{A_x}\frac{\partial w}{\partial x} + A_x\frac{\partial}{\partial z}\left(\frac{u}{A_x}\right)$$

$$\gamma_{yz} = \frac{1}{A_y}\frac{\partial w}{\partial y} + A_y \frac{\partial}{\partial z}\left(\frac{v}{A_y}\right) \tag{17}$$

where $A_x = a_x\left(1 + \frac{z}{R_1}\right)$ and $A_y = a_y\left(1 + \frac{z}{R_2}\right)$ are Lame coefficients. According to the FSDT, the displacements of the structures are given by

$$\begin{aligned} u(x,y,z) &= u_0(x,y) + z\beta_x(x,y) \\ v(x,y,z) &= v_0(x,y) + z\beta_y(x,y) \quad \text{or} \quad \bar{\mathbf{u}} = \mathbf{u}_0 + z\mathbf{u}_1 \\ w(x,y,z) &= w_0(x,y) \end{aligned} \tag{18}$$

and

$$\bar{\mathbf{u}} = \begin{Bmatrix} u \\ v \\ w \end{Bmatrix}; \mathbf{u}_0 = \begin{Bmatrix} u_0 \\ v_0 \\ w_0 \end{Bmatrix}; \quad \mathbf{u}_1 = \begin{Bmatrix} \beta_x \\ \beta_y \\ 0 \end{Bmatrix} \tag{19}$$

where u_0 and v_0 are the tangential displacements, and w_0 is the radial displacement. In addition, β_x and β_y, respectively, are the rotations in y and x axes. For shallow shells, we can assume the following: $a_{x,y} = a_{y,x} = 0$ (constant radii of curvatures), $(1 + z/R_1) \approx 1$ and $(1 + z/R_2) \approx 1$. By using Eq. (18) in Eqs. (16) and (17), the Sanders' strains are re-expressed in the vector form as [59]

$$\begin{aligned} \boldsymbol{\varepsilon} &= \begin{Bmatrix} \varepsilon_{xx} & \varepsilon_{yy} & \gamma_{xy} \end{Bmatrix}^T = \boldsymbol{\varepsilon}_0 + z\boldsymbol{\kappa}_b \\ \boldsymbol{\gamma} &= \begin{Bmatrix} \gamma_{xz} & \gamma_{yz} \end{Bmatrix}^T = \boldsymbol{\varepsilon}_s \end{aligned} \tag{20}$$

where

$$\boldsymbol{\varepsilon}_0 = \begin{Bmatrix} u_{0,x} + \dfrac{w_0}{R_1} \\ v_{0,y} + \dfrac{w_0}{R_2} \\ u_{0,y} + v_{0,x} \end{Bmatrix}; \quad \boldsymbol{\kappa}_b = \begin{Bmatrix} \beta_{x,x} \\ \beta_{y,y} \\ \beta_{x,y} + \beta_{y,x} \end{Bmatrix}; \quad \boldsymbol{\varepsilon}_s = \begin{Bmatrix} -\dfrac{u_0}{R_1} + w_{0,x} + \beta_x \\ -\dfrac{v_0}{R_2} + w_{0,y} + \beta_y \end{Bmatrix} \tag{21}$$

The constitutive equation is written based on Hooke's law as follows [59]:

$$\begin{Bmatrix} \sigma_{xx} \\ \sigma_{yy} \\ \tau_{xy} \\ \tau_{xz} \\ \tau_{yz} \end{Bmatrix} = \begin{bmatrix} Q_{11} & Q_{12} & 0 & 0 & 0 \\ Q_{21} & Q_{22} & 0 & 0 & 0 \\ 0 & 0 & Q_{66} & 0 & 0 \\ 0 & 0 & 0 & Q_{55} & 0 \\ 0 & 0 & 0 & 0 & Q_{44} \end{bmatrix} \begin{Bmatrix} \varepsilon_{xx} \\ \varepsilon_{yy} \\ \gamma_{xy} \\ \gamma_{xz} \\ \gamma_{yz} \end{Bmatrix} \tag{22}$$

and

$$\begin{aligned} &Q_{11} = \frac{E_{11}}{1 - \upsilon_{12}\upsilon_{21}}; \quad Q_{12} = \frac{\upsilon_{12}E_{22}}{1 - \upsilon_{12}\upsilon_{21}}; \quad Q_{22} = \frac{E_{22}}{1 - \upsilon_{12}\upsilon_{21}} \\ &Q_{66} = G_{12}; \quad Q_{55} = G_{13}; \quad Q_{44} = G_{23} \end{aligned} \tag{23}$$

A Galerkin weak form derived from the motion equations for free vibration analysis is expressed as follows

$$\int_{\Omega} \delta \begin{Bmatrix} \boldsymbol{\varepsilon}_0 \\ \boldsymbol{\kappa}_b \end{Bmatrix}^T \begin{bmatrix} \mathbf{A} & \mathbf{B} \\ \mathbf{B} & \mathbf{D}^b \end{bmatrix} \begin{Bmatrix} \boldsymbol{\varepsilon}_0 \\ \boldsymbol{\kappa}_b \end{Bmatrix} \mathrm{d}\Omega + \int_{\Omega} \delta \boldsymbol{\varepsilon}_s^T \mathbf{D}^s \boldsymbol{\varepsilon}_s \mathrm{d}\Omega + \\ + \int_{\Omega} \delta \begin{Bmatrix} \mathbf{u}_0 \\ \mathbf{u}_1 \end{Bmatrix}^T \begin{bmatrix} I_1 & I_2 \\ I_2 & I_3 \end{bmatrix} \begin{Bmatrix} \ddot{\mathbf{u}}_0 \\ \ddot{\mathbf{u}}_1 \end{Bmatrix} \mathrm{d}\Omega = \mathbf{0} \tag{24}$$

where

$$(I_1, I_2, I_3) = \int_{-h/2}^{h/2} \rho(z) \left(1, z, z^2\right) \mathrm{d}z \tag{25}$$

$$(A_{ij}, B_{ij}, D_{ij}^b) = \int_{-h/2}^{h/2} (1, z, z^2) Q_{ij} \mathrm{d}z; \quad i, j = 1, 2, 6 \\ D_{ij}^s = \kappa \int_{-h/2}^{h/2} Q_{ij} \mathrm{d}z; \quad i, j = 4, 5 \tag{26}$$

and the shear correction factor $\kappa = 5/6$.

3 The FGM-FGCNTRC Sandwich Shell Formulation Using the Meshfree MK Method and FSDT

3.1 Improved Meshfree MK Method

We consider a domain Ω with the boundary Γ and an arbitrary point $\mathbf{x}$ inside Ω. The support domain of point $\mathbf{x}$, $\Omega_{\mathbf{x}}$, which contains n nodes, is shown in Fig. 5 ($\Omega_{\mathbf{x}} \in \Omega$). The MK approximation is expressed as follows [35]

$$\mathbf{u}^h(\mathbf{x}) = [\mathbf{p}^T(\mathbf{x})\mathbf{A} + \mathbf{r}^T(\mathbf{x})\mathbf{B}]\mathbf{u} \tag{27}$$

where

$$\mathbf{p}(\mathbf{x}) = \{p_1(\mathbf{x}) \quad p_2(\mathbf{x}) \quad p_3(\mathbf{x}) \quad \ldots \quad p_m(\mathbf{x})\}^T \\ \mathbf{A} = (\mathbf{P}^T\mathbf{R}^{-1}\mathbf{P})^{-1}\mathbf{P}^T\mathbf{R}^{-1} \\ \mathbf{B} = \mathbf{R}^{-1}(\mathbf{I} - \mathbf{P}\mathbf{A}) \tag{28}$$

in which, $\mathbf{p}(\mathbf{x})$ is a polynomial. In this article, the second-order polynomial is chosen to establish the MK shape functions. The quantity $\mathbf{u}$ is the displacement vector, and $\mathbf{u}^h(\mathbf{x})$ is the approximate value of this vector at point $\mathbf{x}$. The matrix $\mathbf{P}$ is achieved from the polynomial as follows

$$\mathbf{p} = \begin{bmatrix} p_1(\mathbf{x}_1) & \ldots & p_m(\mathbf{x}_1) \\ \ldots & \ldots & \ldots \\ p_1(\mathbf{x}_n) & \ldots & p_m(\mathbf{x}_n) \end{bmatrix} \tag{29}$$

where $\mathbf{r}^T(\mathbf{x})$ includes the n correlation functions $R(\mathbf{x}_i, \mathbf{x})$ between point $\mathbf{x}$ and node $\mathbf{x}_i$ inside the support domain $\Omega_{\mathbf{x}}$, computed as

$$\mathbf{r}(\mathbf{x}) = \{R(\mathbf{x}_1, \mathbf{x}) \quad R(\mathbf{x}_2, \mathbf{x}) \quad \cdots \quad R(\mathbf{x}_n, \mathbf{x})\}^T \tag{30}$$

and

$$\mathbf{R} = \begin{bmatrix} R(\mathbf{x}_1, \mathbf{x}_1) & \dots & R(\mathbf{x}_1, \mathbf{x}_n) \\ \dots & \dots & \dots \\ R(\mathbf{x}_n, \mathbf{x}_1) & \dots & R(\mathbf{x}_n, \mathbf{x}_n) \end{bmatrix} \tag{31}$$

The MK approximation also can be re-expressed in another form as follows [35]

$$\mathbf{u}^h(\mathbf{x}) = \sum_{1}^{n} N_I(\mathbf{x}) u_I \tag{32}$$

where $N_I(\mathbf{x})$ is the MK interpolation function (or the MK shape function) given by

$$N_I(\mathbf{x}) = \sum_{j=1}^{m} p_j(\mathbf{x}) A_{jI} + \sum_{k=1}^{n} r_k(\mathbf{x}) B_{kI} \tag{33}$$

where the first- and second-order derivatives of the MK shape functions are given by

$$\begin{aligned} N_{I,\alpha}(\mathbf{x}) &= \sum_{j=1}^{m} p_{j,\alpha}(\mathbf{x}) A_{jI} + \sum_{k=1}^{n} r_{k,\alpha}(\mathbf{x}) B_{kI} \\ N_{I,\alpha\alpha}(\mathbf{x}) &= \sum_{j=1}^{m} p_{j,\alpha\alpha}(\mathbf{x}) A_{jI} + \sum_{k=1}^{n} r_{k,\alpha\alpha}(\mathbf{x}) B_{kI} \end{aligned} \tag{34}$$

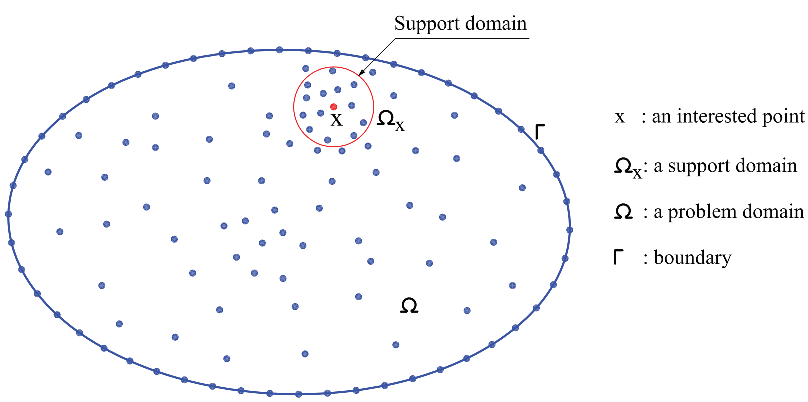

Figure 5: Discretization and support domain of a 2D problem utilizing the meshless moving-Kriging method

An improved meshfree MK method was proposed in [35] to ensure that the MK solutions remain stable and accurate. This improved method uses a quartic-spline correlation function to establish the MK shape functions as

$$R(\mathbf{x}_I, \mathbf{x}_J) = 1 - 6\left(\frac{\theta r_{IJ}}{a_0}\right)^2 + 8\left(\frac{\theta r_{IJ}}{a_0}\right)^3 - 3\left(\frac{\theta r_{IJ}}{a_0}\right)^4; \quad \left(0 \le \frac{\theta r_{IJ}}{a_0} \le 1\right) \tag{35}$$

where a_0 is the maximum distance between the computational point $\mathbf{x}$ and the farthest node in its support domain, and θ is the correlation parameter. As numerically demonstrated, the MK shape functions and the solutions obtained using the improved meshfree MK method are independent of changes in θ [35]. Thus, θ

can be fixed at 1 in the numerical implementations in this article. In addition, r_{IJ} is the Euclidean distance between points $\mathbf{x}_I$ and $\mathbf{x}_J$, which is given by

$$r_{IJ} = \|\mathbf{x}_I - \mathbf{x}_J\| \tag{36}$$

The MK shape functions satisfy the Kronecker-delta property. Thus, the essential boundary conditions are simply and straightforwardly imposed as in the FEM. Notably, the main computational procedures of the improved meshfree MK method and the FEM are the same. In meshfree methods, a support domain is utilized to determine a set of nodes that are used for constructing the shape functions. In this article, the support domain with a circular shape as shown in Fig. 5 is utilized. The radius of this circle is determined as follows:

$$d_m = \alpha d_c \tag{37}$$

here, d_c is a characteristic length, which is the node spacing in cases with regularly distributed nodes, and α is a scale factor, with $\alpha = [2 \div 4]$ for elastic problems [35]. The higher the scale factor, the more nodes collected in the support domain. As a result, the computational cost can be high. Accordingly, α is fixed at 2.4 for all problems in this article for the balance between the accuracy and efficiency of the method.

3.2 The FGM-FGCNTRC Sandwich Shell Formulation Using the Meshfree MK Method

The displacement field $\mathbf{u}$ of shells can be approximated using the MK interpolation functions as follows

$$\mathbf{u}^h(x, y) = \sum_{A=1}^{n} N_A(x, y)\mathbf{q}_A \tag{38}$$

where $N_A(x, y)$ is the MK interpolation function, $\mathbf{q}_A = \left\{ u_{0A} \quad v_{0A} \quad w_{0A} \quad \beta_{xA} \quad \beta_{yA} \right\}^T$ is a vector containing degrees of freedom of node A, and $\mathbf{u}^h$ is the vector including the approximate displacements. Inserting Eq. (38) into Eq. (21), the membrane, bending, and shear strains are, respectively, expressed in terms of the displacements as

$$\boldsymbol{\varepsilon}_0 = \sum_{A=1}^{n} \mathbf{B}_A^0\mathbf{q}_A; \quad \boldsymbol{\kappa}_b = \sum_{A=1}^{n} \mathbf{B}_A^b\mathbf{q}_A; \quad \boldsymbol{\varepsilon}_s = \sum_{A=1}^{n} \mathbf{B}_A^s\mathbf{q}_A \tag{39}$$

where

$$\mathbf{B}_A^0 = \begin{bmatrix} N_{A,x} & 0 & \frac{1}{R_1}N_A & 0 & 0 \\ 0 & N_{A,y} & \frac{1}{R_2}N_A & 0 & 0 \\ N_{A,y} & N_{A,x} & 0 & 0 & 0 \end{bmatrix}; \quad \mathbf{B}_A^b = \begin{bmatrix} 0 & 0 & 0 & N_{A,x} & 0 \\ 0 & 0 & 0 & 0 & N_{A,y} \\ 0 & 0 & 0 & N_{A,y} & N_{A,x} \end{bmatrix}$$
$$\mathbf{B}_A^s = \begin{bmatrix} -\frac{1}{R_1}N_A & 0 & N_{A,x} & N_A & 0 \\ 0 & -\frac{1}{R_2}N_A & N_{A,y} & 0 & N_A \end{bmatrix} \tag{40}$$

Eq. (38) is inserted into Eq. (19), we obtain the approximate displacement vectors as

$$\mathbf{u}_0 = \sum_{A=1}^{n} \mathbf{N}_A^0\mathbf{q}_A; \quad \mathbf{u}_1 = \sum_{A=1}^{n} \mathbf{N}_A^1\mathbf{q}_A \tag{41}$$

where

$$\mathbf{N}_A^0 = \begin{bmatrix} N_A & 0 & 0 & 0 & 0 \\ 0 & N_A & 0 & 0 & 0 \\ 0 & 0 & N_A & 0 & 0 \end{bmatrix}; \quad \mathbf{N}_A^1 = \begin{bmatrix} 0 & 0 & 0 & N_A & 0 \\ 0 & 0 & 0 & 0 & N_A \\ 0 & 0 & 0 & 0 & 0 \end{bmatrix} \tag{42}$$

Finally, by using Eqs. (39) and (41) in Eq. (24), the discretized system of equations for free vibration analysis of FGM-FGCNTRC sandwich shells based on MK meshfree method and FSDT is achieved as

$$\left(\mathbf{K} - \omega^2\mathbf{M}\right)\mathbf{q} = \mathbf{0} \tag{43}$$

where $\mathbf{K}$ and $\mathbf{M}$ are, respectively, the global stiffness and mass matrices as follows

$$\begin{aligned} \mathbf{K} &= \int_\Omega \left(\begin{Bmatrix} \mathbf{B}^0 \\ \mathbf{B}^b \end{Bmatrix}^T \begin{bmatrix} \mathbf{A} & \mathbf{B} \\ \mathbf{B} & \mathbf{D}^b \end{bmatrix} \begin{Bmatrix} \mathbf{B}^0 \\ \mathbf{B}^b \end{Bmatrix} + (\mathbf{B}^s)^T \mathbf{D}^s \mathbf{B}^s \right) \mathrm{d}\Omega \\ \mathbf{M} &= \int_\Omega \begin{Bmatrix} \mathbf{N}^0 \\ \mathbf{N}^1 \end{Bmatrix}^T \begin{bmatrix} I_1 & I_2 \\ I_2 & I_3 \end{bmatrix} \begin{Bmatrix} \mathbf{N}^0 \\ \mathbf{N}^1 \end{Bmatrix} \mathrm{d}\Omega \end{aligned} \tag{44}$$

4 Results and Discussion

For the FGCNTRC core, the matrix material is Poly methyl methacrylate (PMMA) [61] and the reinforcements are the armchair $(10, 10)$ single-walled carbon nanotubes [50]. Unless otherwise stated, the parameters of the CNTs are as provided in [50]

- $V_{CNT}^* = 0.11$: $\eta_1 = 0.149$ and $\eta_2 = 0.934$
- $V_{CNT}^* = 0.14$: $\eta_1 = 0.150$ and $\eta_2 = 0.941$
- $V_{CNT}^* = 0.17$: $\eta_1 = 0.149$ and $\eta_2 = 1.381$

It is assumed that $\eta_3 = \eta_2$ and $G_{12} = G_{13} = G_{23}$. The mechanical properties of materials are provided as follows

- The matrix material
  $E^m = (3.52 - 0.0034T)$ GPa, $\nu^m = 0.34$, $\rho^m = 1150\text{kg/m}^3$, $T = T_0 + \Delta T$, $T_0 = 300\text{K}$
- The reinforcement material
  $E_{11}^{CNT} = 5.6466$ TPa, $E_{22}^{CNT} = 7.0800$ TPa, $G_{12}^{CNT} = 1.9445$ TPa, $\nu_{12}^{CNT} = 0.175$, $\rho^{CNT} = 1400\,\text{kg/m}^3$

For the FGM skins, Al and Al_2O_3 were respectively chosen as the metal and ceramic materials. Their mechanical properties are given as the following: $E = 70$ GPa, $\nu = 0.3$, $\rho = 2707$ kg/m^3 (for Al); $E = 380$ GPa, $\nu = 0.3$, and $\rho = 3800$ kg/m^3 (for Al_2O_3). As mentioned earlier, the rule of mixture was used to compute the effective properties of both the FGCNTRC core and the FGM skins. For the typical shell shown in Fig. 6, we investigate two types of boundary conditions:

- Simply supported (S)

$$\begin{aligned} &u_0 = w_0 = \beta_x = 0 \quad \text{at} \quad y = 0, L \\ &v_0 = w_0 = \beta_y = 0 \quad \text{at} \quad x = 0, \alpha R \end{aligned} \tag{45}$$

- Clamped (C)

$$u_0 = v_0 = w_0 = \beta_x = \beta_y = 0 \tag{46}$$

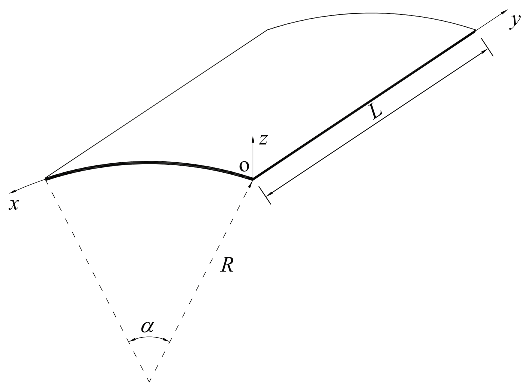

Figure 6: Geometry of a cylindrical shell

In this article, boundary conditions were enforced as in the standard FEM. A mesh of 27 × 27 nodes was used for all problems, and numerical integration was performed utilizing 4 × 4 Gaussian points per each background structure cell. The computational meshes for cylindrical, spherical, and hyperbolic parabolic shells are shown in Fig. 7. Notably, the two key parameters investigated in section Parameter study are defined as the thickness-to-radius ratio (h/R) and the length-to-radius ratio (L/R).

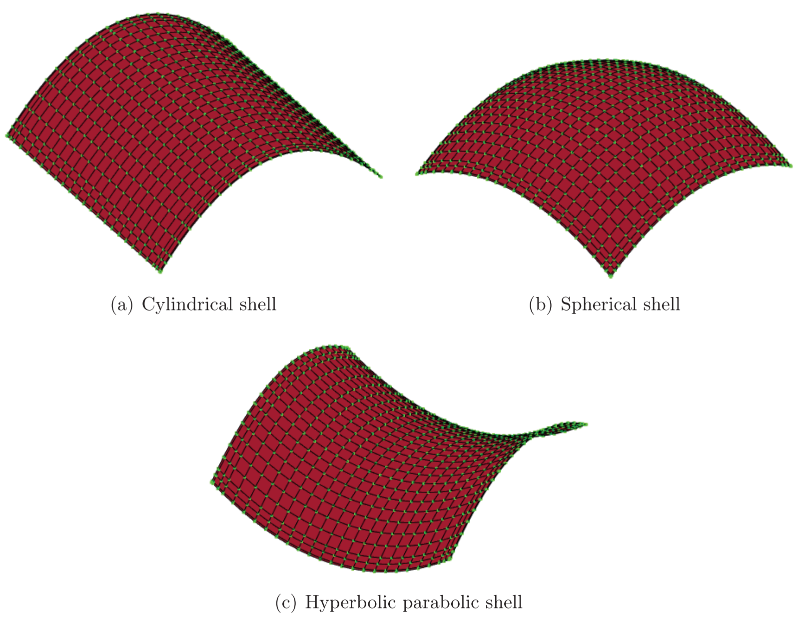

Figure 7: Structural discretization utilizing the meshless moving-Kriging method

4.1 Verification Study

Notably, this is the first study on free-vibration analysis of FGM-FGCNTRC sandwich shells. Thus, solutions for these proposed structures are not available in the literature. However, because square FGM sandwich plates, cylindrical FGCNTRC shells, isotropic spherical and hyperbolic-parabolic shells are particular cases of doubly curved FGM-FGCNTRC sandwich shells. Therefore, the accuracy of the present formulation is, respectively, confirmed by performing free vibration analyses of these structures. Notably, the mechanical properties of FGM and FGCNTRC have been provided at the beginning of this section. In particular, by setting the thicknesses of the two skin layers to zero, the present formulation can be applied to structures with only one layer. This numerical implementation is very simple and can be done quickly using our in-house MATLAB codes.

4.1.1 Square Sandwich Plates with FGM Skins and an Isotropic Core

A square plate is a particular case of a doubly curved shell, with $R_1 = R_2 = \infty$. A fully simply supported (SSSS) sandwich square plate ($a/b = 1$ and $a/h = 10$) is first investigated. This sandwich plate consists of FGM skins and a pure ceramic core. The FGM skins (Al/Al_2O_3) are metal-rich at the top and bottom surfaces. The normalized frequency is defined as $\bar{\omega} = \omega a^2/h$. Table 1 shows the first normalized frequencies of the plates with various power-law indices n and layer-thickness ratios. As seen, the present results well agree with those obtained using 3D elasticity [3]. The high accuracy of the present formulation for analyses of sandwich plates with FGM skins and isotropic cores is confirmed.

Table 1: First normalized frequencies of SSSS sandwich square plates, $a/h = 10$

n	Method	1-0-1	2-1-2	1-1-1	1-2-1
0.5	3D elasticity [3]	1.4461	1.4861	1.5213	1.5766
	Present	1.4442	1.4842	1.5196	1.5755
1	3D elasticity [3]	1.2447	1.3018	1.3552	1.4413
	Present	1.2425	1.2995	1.3531	1.4397
5	3D elasticity [3]	0.9448	0.9810	1.0453	1.1757
	Present	0.9442	0.9804	1.0437	1.1736
10	3D elasticity [3]	0.9273	0.9418	0.9952	1.1247
	Present	0.9267	0.9413	0.9943	1.1226

4.1.2 Cylindrical FGCNTRC Shells

Next, we verify the present formulation for the analysis of cylindrical FGCNTRC shells. A cylindrical FGCNTRC panel is shown in Fig. 6, and its geometric properties are $\alpha = 0.1$ rad, $h/R = 0.002$, $R = 1$ m, and $L/R = 0.1$. The results we obtained include the first six normalized frequencies of the panels, which are listed in Table 2 for various types of CNT distributions and boundaries. Here again, the present results agree well with those obtained using the meshfree KP-Ritz method (MKR) [61]. The high accuracy of the present formulation for the analysis of cylindrical FGCNTRC shells is confirmed.

4.1.3 Isotropic Spherical and Hyperbolic-PARabolic Shells

We next carried out a verification of the present formulation for the analysis of isotropic spherical and hyperbolic-parabolic shells. The doubly-curved shell shown in Fig. 8 is considered. Here, Poisson's ratio is fixed at $\nu = 0.3$ and the length-to-thickness ratio is fixed at $L_y/h = 100$. The shell is fully clamped (CCCC) at its boundaries. The non-dimensional frequency parameter is defined as $\lambda = \omega L_x L_y \sqrt{\rho h/D}$, with $D = Eh^3/12(1-\nu^2)$. Table 3 shows the first six normalized frequencies of the spherical and hyperbolic-parabolic shells. Notably, the spherical shells correspond to the radii $R_x = R_y = 1$ m while the hyperbolic-parabolic ones correspond to $R_x = 1$ m and $R_y = -1$ m. As seen, the present results agree well with those obtained using the pb-2 Ritz method [62]. The high accuracy of the present formulation for the analysis of isotropic spherical and hyperbolic parabolic shells is confirmed.

Table 2: First six normalized frequencies of cylindrical FG-CNTRC shells, $L/R = 0.1$, $h/R = 0.002$, $V^*_{CNT} = 0.11$

	Mode	CNT distributions							
		UD		FG-V		FG-O		FG-X	
		Present	MKR [61]	Present	MKR [61]	Present	MKR [61]	Present	MKR [61]
SSSS	1	17.985	17.850	15.408	15.273	13.577	13.444	21.407	21.243
	2	22.300	22.073	20.437	20.183	18.735	18.482	25.349	25.096
	3	33.684	33.285	32.671	32.257	31.005	30.587	36.328	35.939
	4	52.485	51.778	52.089	51.410	49.084	48.702	55.159	54.535
	5	65.592	65.121	55.704	55.300	50.122	49.430	77.285	76.758
	6	67.958	67.264	58.682	58.006	52.150	51.505	79.368	78.556
CCCC	1	37.299	36.849	32.088	31.690	28.542	28.172	43.442	42.937
	2	41.588	40.924	37.182	36.567	33.793	33.213	47.366	46.640
	3	52.749	51.825	49.564	48.692	46.429	45.593	57.942	56.946
	4	71.911	70.638	69.906	68.671	66.716	65.505	76.734	75.394
	5	92.194	91.445	80.482	79.804	72.055	71.419	103.773	101.720
	6	94.862	93.611	83.748	82.583	75.456	74.350	104.835	104.000

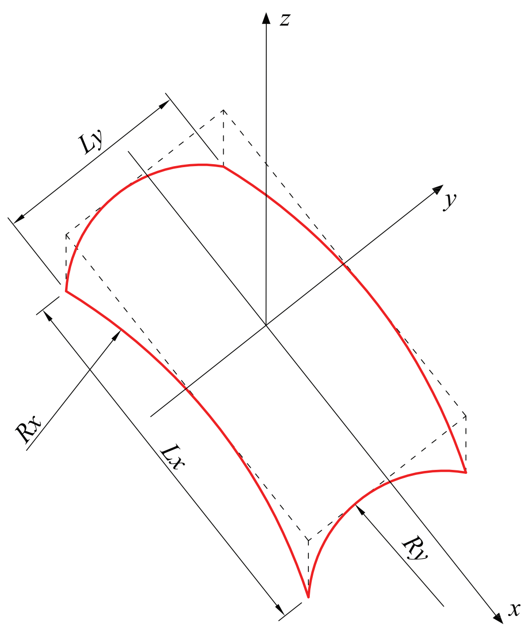

Figure 8: Geometry of a doubly-curved shell

Table 3: First six non-dimensional frequency parameters λ of CCCC thin shells with $\nu = 0.3$ and $L_y/h = 100$

L_x/L_y	b/R_y	R_y/R_x	Method	Mode					
				1	2	3	4	5	6
1	0.1	−1	Ritz [62]	50.750	79.151	79.151	110.690	135.260	135.730
			Present	50.396	80.041	80.041	112.328	138.752	139.170
		1	Ritz [62]	58.297	81.755	81.755	114.160	136.010	137.720
			Present	58.746	82.641	82.641	115.755	139.498	141.257
	0.5	−1	Ritz [62]	157.350	157.350	157.410	166.520	204.030	208.690
			Present	156.315	156.315	156.460	165.117	204.459	207.396
		1	Ritz [62]	191.990	191.990	196.930	209.960	216.190	242.220
			Present	190.606	190.606	196.245	209.258	216.726	243.609
2	0.1	−1	Ritz [62]	87.160	89.709	108.320	139.630	141.880	151.240
			Present	86.048	89.183	108.123	141.024	143.590	154.213
		1	Ritz [62]	102.220	103.080	118.760	144.820	145.640	158.670
			Present	102.426	103.572	119.332	146.495	147.229	161.583
	0.5	−1	Ritz [62]	262.080	262.400	278.370	279.800	308.700	311.030
			Present	258.283	259.186	276.155	278.366	307.152	311.247
		1	Ritz [62]	358.830	359.790	360.940	375.760	379.230	385.010
			Present	354.878	357.146	358.327	372.658	379.051	385.034

4.2 Parameter Study

4.2.1 Cylindrical FGM-FGCNTRC Sandwich Shells

We next consider the cylindrical FGM-FGCNTRC sandwich shell shown in Fig. 6. Its geometric properties are $\alpha = 0.1$ rad, $R = 1$ m, $L/R = 0.1$, and the shell is fully clamped (CCCC) at its boundaries. The normalized frequency is computed as $\hat{\omega} = 10\omega L^2\sqrt{\rho^m/E^m}$, where ρ^m and E^m are the mechanical properties of the matrix material of the FGCNTRC core. Table 4 presents the first normalized frequencies of shells with the power-law index $n = 1$, the layer-thickness ratio 1-2-1, various types of CNT distributions, values of V^*_{CNT}, and thickness-to-radius ratios (h/R). As seen, the higher the thickness-to-radius ratio, the higher the stiffness and frequency of the shell. The results in Table 4 are visualized in Fig. 9. It is seen that the greater the quantity of CNTs, the higher the stiffness and frequency of the shell. FG-X is the best CNT distribution which produces the highest stiffness and frequency of the shell compared to the rest CNT distributions. FG-nX (proposed) produces a higher stiffness and frequency of the shell than do the distributions UD, FG-V, and FG-O. Table 5 shows the first six normalized frequencies of shells with various boundaries, power-law indices, and length-to-radius ratios (L/R). It is found that when more constraints are applied at the boundaries, the higher the frequency of the shell. The higher the length-to-radius ratio, the higher the stiffness and frequency of the shell. Note that R was fixed at 1 m for these calculations. The higher the power-law index n, the lower is the amount of ceramic in the shell, which produces the frequency of the shell. Fig. 10 shows the first six mode shapes of a cylindrical CCCC FGM-FGCNTRC sandwich shell with $L/R = 0.1$ and $n = 1$. Table 6 lists the first normalized frequencies of cylindrical CCCC FGM-FGCNTRC sandwich shells with various power-law indices, CNT distributions, and layer-thickness ratios. It is seen that the thicker the FGCNTRC core, the higher the stiffness and frequency of the shell. The results in Table 6 are visualized in Fig. 11. It is found that the effect of the CNT distribution on the frequency of the shell is very small for the layer-thickness ratio

2-1-2, while it is significant for the case layer-thickness ratio 1-2-1. It is recommended to use cylindrical FGM-FGCNTRC sandwich shells with the layer-thickness ratio 1-2-1 (or shells with thicker FGCNTRC cores) to efficiently exploit the CNT distribution.

Table 4: First normalized frequencies of CCCC cylindrical FGM-FGCNTRC sandwich shells with R = 1 m, L/R = 0.1, n = 1 and the layer-thickness ratio 1-2-1

h/R	CNT distributions	V^*_{CNT}		
		0.11	**0.14**	**0.17**
0.004	UD	2.578	2.583	2.590
	FG-V	2.574	2.578	2.583
	FG-O	2.563	2.565	2.568
	FG-X	2.592	2.602	2.612
	FG-nX	2.589	2.598	2.607
0.008	UD	4.754	4.763	4.776
	FG-V	4.748	4.755	4.765
	FG-O	4.730	4.733	4.739
	FG-X	4.778	4.794	4.812
	FG-nX	4.772	4.787	4.804

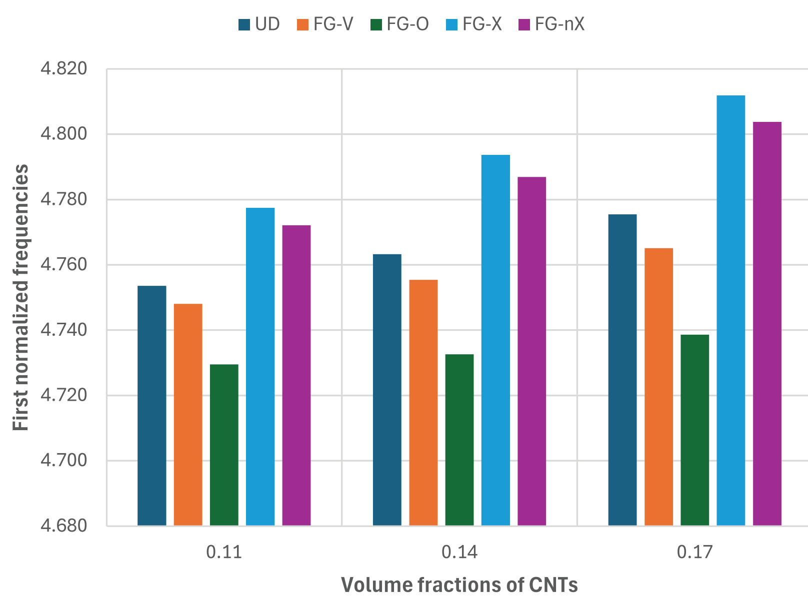

Figure 9: Effect of the CNT distribution on the first normalized frequency of the cylindrical FGM-FGCNTRC sandwich shell with h/R = 0.008, R = 1 m, L/R = 0.1, n = 1 and the layer-thickness ratio 1-2-1

Table 5: First six normalized frequencies of cylindrical FGM-FGCNTRC sandwich shells with R = 1 m, h/R = 0.008, V^*_{CNT} = 0.11, UD distribution and the layer-thickness ratio 1-2-1

Boundary	L/R	n	Mode					
			1	2	3	4	5	6
SSSS	0.1	0.5	3.084	7.306	7.406	10.261	10.265	11.332
		1	2.768	6.561	6.675	9.451	9.455	10.205
		5	2.098	4.951	5.112	7.289	7.292	7.751
		10	1.956	4.600	4.772	6.632	6.635	7.204
	0.2	0.5	7.752	12.280	19.339	20.378	25.245	28.309
		1	6.944	11.023	17.398	18.771	22.654	25.514
		5	5.232	8.355	13.265	14.477	17.074	19.532
		10	4.869	7.788	12.381	13.172	15.862	18.235
CCCC	0.1	0.5	5.275	9.968	10.081	14.116	16.454	16.708
		1	4.754	8.988	9.120	12.764	14.876	15.153
		5	3.622	6.814	7.000	9.732	11.292	11.657
		10	3.370	6.315	6.512	9.020	10.439	10.823
	0.2	0.5	14.755	18.793	25.539	34.299	35.476	39.153
		1	13.259	16.913	23.026	30.974	31.958	35.292
		5	10.016	12.839	17.573	23.727	24.169	26.728
		10	9.302	11.940	16.363	22.102	22.390	24.764

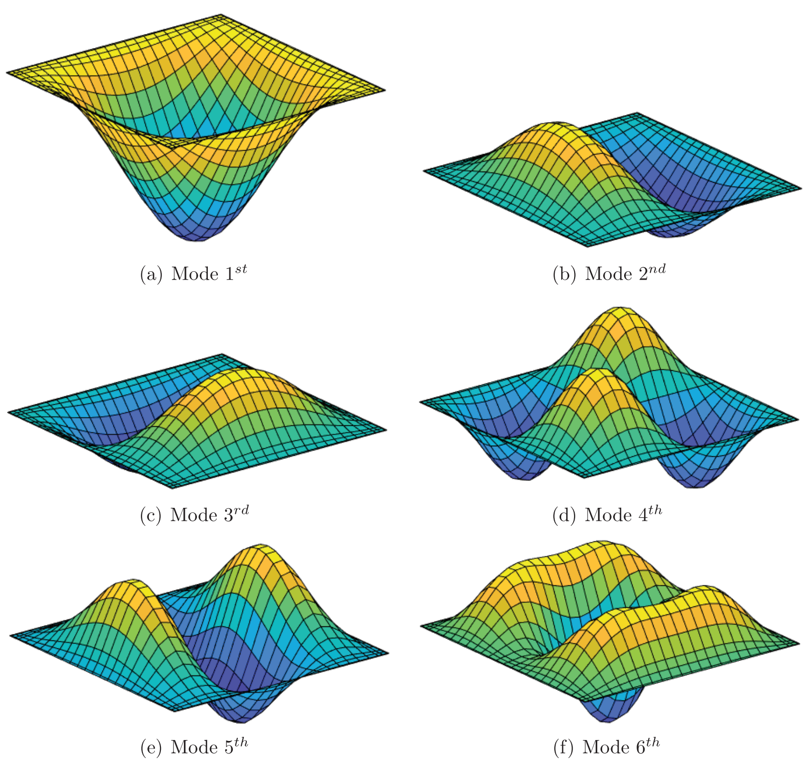

(a) Mode 1^{st} (b) Mode 2^{nd} (c) Mode 3^{rd} (d) Mode 4^{th} (e) Mode 5^{th} (f) Mode 6^{th}

Figure 10: First six mode shapes of a cylindrical FGM-FGCNTRC sandwich shell

Table 6: First normalized frequencies of CCCC cylindrical FGM-FGCNTRC sandwich shells with R = 1 m, L/R = 0.1, h/R = 0.008, V_{CNT}^{*} = 0.11

n	CNT distributions	2-1-2	1-1-1	1-2-1
0.5	UD	4.830	5.072	5.275
	FG-V	4.829	5.071	5.271
	FG-O	4.828	5.067	5.255
	FG-X	4.831	5.078	5.296
	FG-nX	4.831	5.079	5.077
1	UD	4.251	4.516	4.754
	FG-V	4.251	4.515	4.748
	FG-O	4.250	4.509	4.730
	FG-X	4.253	4.523	4.778
	FG-nX	4.252	4.522	4.772
5	UD	3.208	3.416	3.622
	FG-V	3.208	3.413	3.611
	FG-O	3.206	3.405	3.587
	FG-X	3.211	3.426	3.656
	FG-nX	3.210	3.424	3.648
10	UD	3.063	3.217	3.370
	FG-V	3.063	3.214	3.358
	FG-O	3.061	3.206	3.333
	FG-X	3.066	3.228	3.407
	FG-nX	3.065	3.226	3.399

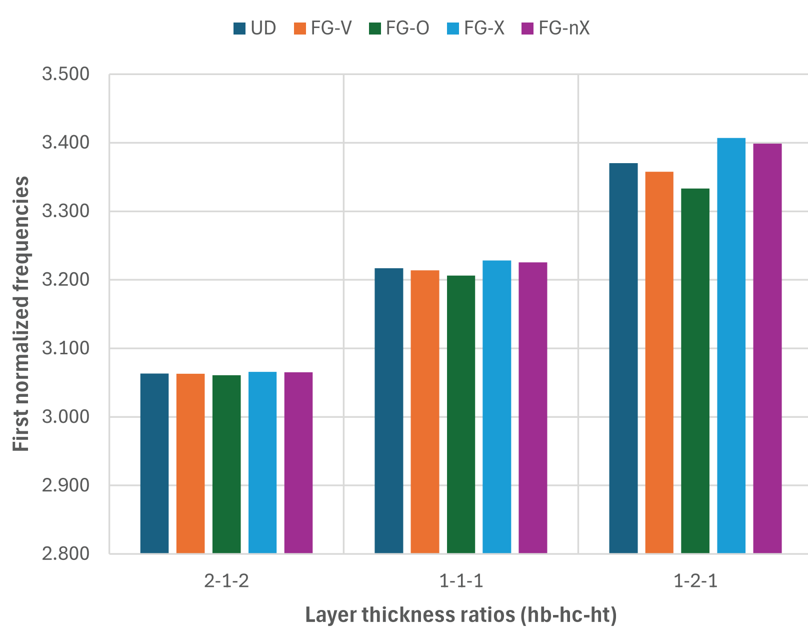

Figure 11: Effect of the layer-thickness ratio on the first normalized frequency of the cylindrical FGM-FGCNTRC sandwich shell with h/R = 0.008, R = 1 m, L/R = 0.1, n = 10, V_{CNT}^{*} = 0.11

4.2.2 Spherical FGM-FGCNTRC Sandwich Shells

The spherical FGM-FGCNTRC sandwich shell shown in Fig. 8 is next considered. Its geometric properties are $R_x = R_y = 1$ m, $L_y/R_y = 0.1$, and $L_x = L_y$. The normalized frequency is $\hat{\omega} = 10\omega L_y^2\sqrt{\rho^m/E^m}$, where ρ^m and E^m are again the mechanical properties of the matrix material of the FGCNTRC core. Table 7 lists the first six normalized frequencies of spherical FGM-FGCNTRC sandwich shells with various boundaries, power-law indices, and thickness-to-radius ratios. Similar to our earlier observations in Section 4.2.1, when more constraints are applied at the boundaries, the higher is the frequency of the shell. The higher the thickness-to-radius ratio, the higher are the stiffness and frequency of the shell. Fig. 12 shows the first six mode shapes of a spherical SSSS FGM-FGCNTRC sandwich shell with $h/R_x = 0.008$ and $n = 1$. As seen, the mode shapes of the spherical shell are quite different from those of the cylindrical shell shown in Fig. 10. Table 8 lists the first normalized frequencies of CCCC shells with various CNT distributions, V^*_{CNT}, power-law indices, and length-to-radius ratios. The results in Table 8 are visualized in Fig. 13 for the case $L_y/R_y = 0.1$ and $n = 1$. It is seen that the higher the length-to-radius ratio or the larger the amount of CNTs, the higher the stiffness and frequency of the shell. Here again, FG-X is the best CNT distribution which produces the highest stiffness and frequency of the shell compared to the rest CNT distributions. FG-nX distribution (proposed) produces a higher stiffness and frequency of the shell than do the distributions UD, FG-V, and FG-O. Table 9 presents the first normalized frequencies of CCCC shells with various CNT distributions, power-law indices, and layer-thickness ratios. The results in Table 9 are visualized in Fig. 14 for the case $n = 10$. It is seen that the thicker the FGCNTRC core, the higher are the stiffness and frequency of the shell. It is found that the effect of CNT distribution on the frequency of the shell is very small for the case layer-thickness ratio 2-1-2, while it is significant for the case layer-thickness ratio 1-2-1. It is recommended to use spherical FGM-FGCNTRC sandwich shells with the layer-thickness ratio 1-2-1 (or shells with thicker FGCNTRC cores) to efficiently exploit the CNT distribution.

Table 7: First six normalized frequencies of spherical FGM-FGCNTRC sandwich shells with $R_x = R_y = 1$ m, $V^*_{CNT} = 0.11$, UD distribution, the layer-thickness ratio 1-2-1, $L_y/R_y = 0.1$, $L_x = L_y$

Boundary	h/R_x	n	**Mode**					
			1	**2**	**3**	**4**	**5**	**6**
SSSS	0.004	0.5	1.663	3.911	3.958	6.207	7.579	7.708
		1	1.495	3.506	3.561	5.572	6.796	6.946
		5	1.136	2.645	2.725	4.223	5.121	5.338
		10	1.057	2.461	2.549	3.936	4.762	4.998
	0.008	0.5	3.116	7.321	7.409	10.260	10.260	11.335
		1	2.798	6.575	6.679	9.451	9.451	10.209
		5	2.122	4.965	5.114	7.289	7.289	7.754
		10	1.977	4.612	4.775	6.632	6.632	7.207
CCCC	0.004	0.5	2.934	5.646	5.713	8.246	9.780	9.951
		1	2.642	5.069	5.148	7.417	8.786	8.980
		5	2.020	3.834	3.947	5.638	6.636	6.906
		10	1.885	3.567	3.690	5.252	6.164	6.456
	0.008	0.5	5.310	9.979	10.080	14.118	16.453	16.710
		1	4.787	8.999	9.120	12.766	14.876	15.154
		5	3.653	6.825	7.000	9.734	11.294	11.658
		10	3.400	6.326	6.512	9.022	10.441	10.824

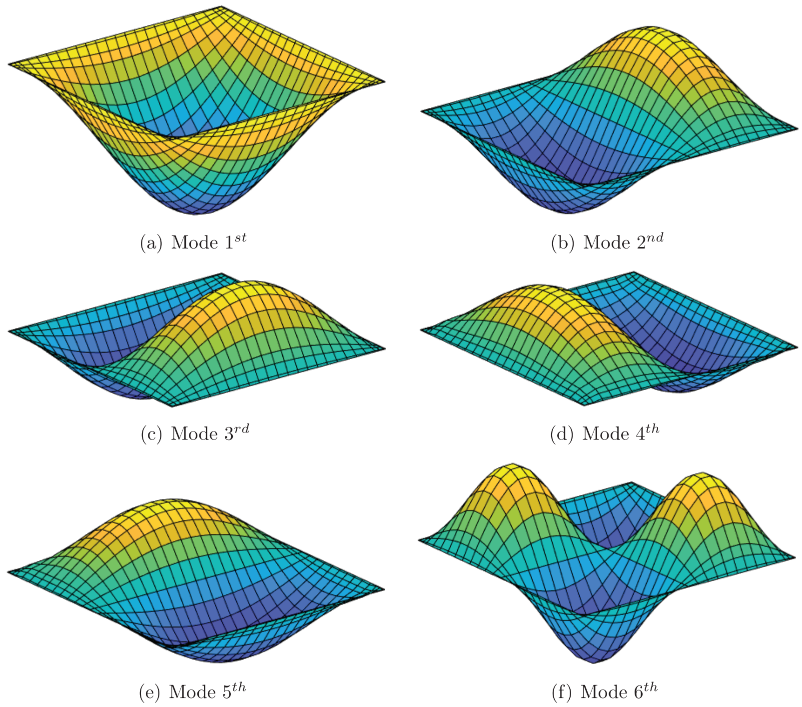

Figure 12: First six mode shapes of a spherical FGM-FGCNTRC sandwich shell

Table 8: First normalized frequencies of CCCC spherical FGM-FGCNTRC sandwich shells with $R_x = R_y = 1$ m, the layer-thickness ratio 1-2-1, $h/R_x = 0.008$, $L_x = L_y$

L_y/R_y	n	CNT distributions	V^*_{CNT}		
			0.11	**0.14**	**0.17**
0.1	1	UD	4.787	4.799	4.813
		FG-V	4.782	4.791	4.803
		FG-O	4.763	4.768	4.776
		FG-X	4.811	4.829	4.849
		FG-nX	4.806	4.822	4.841
	0.5	UD	5.310	5.319	5.330
		FG-V	5.305	5.313	5.322
		FG-O	5.289	5.293	5.299
		FG-X	5.330	5.344	5.361
		FG-nX	5.325	5.339	5.354
0.2	1	UD	5.848	5.883	5.920
		FG-V	5.841	5.874	5.907
		FG-O	5.823	5.851	5.881
		FG-X	5.873	5.915	5.958
		FG-nX	5.868	5.908	5.950

(Continued)

Table 8 (continued)

L_y/R_y	n	CNT distributions	V^*_{CNT}		
			0.11	0.14	0.17
	0.5	UD	6.454	6.483	6.514
		FG-V	6.448	6.476	6.504
		FG-O	6.432	6.456	6.481
		FG-X	6.476	6.511	6.548
		FG-nX	6.471	6.505	6.540

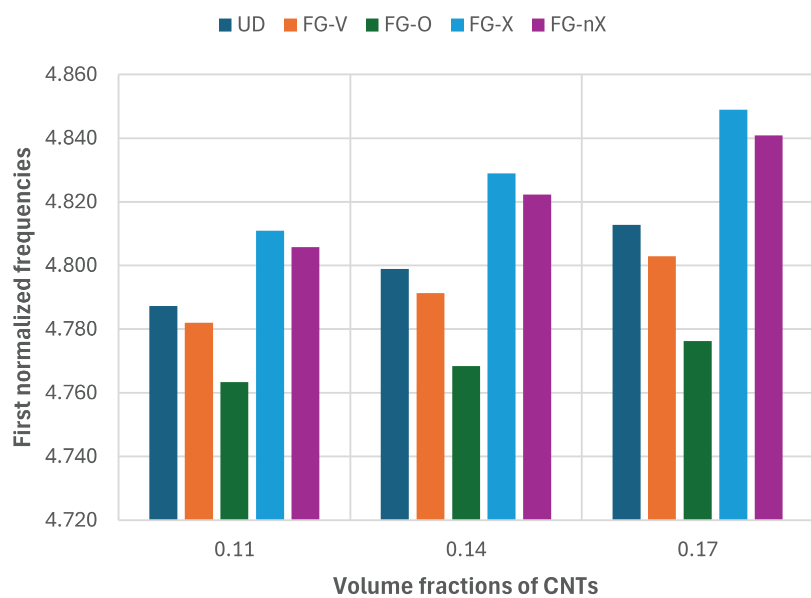

Figure 13: Effect of the CNT distribution on the first normalized frequency of the spherical FGM-FGCNTRC sandwich shell with $h/R_x = 0.008$, $R_x = 1$ m, $R_y = 1$ m, $L_y/R_y = 0.1$, $n = 1$, $L_x = L_y$ and the layer-thickness ratio 1-2-1

Table 9: First normalized frequencies of CCCC spherical FGM-FGCNTRC sandwich shells with $R_x = R_y = 1$ m, $h/R_x = 0.008$, $L_y/R_y = 0.1$, $L_x = L_y$, $V^*_{CNT} = 0.11$

n	CNT distributions	2-1-2	1-1-1	1-2-1
0.5	UD	4.870	5.110	5.310
	FG-V	4.870	5.109	5.305
	FG-O	4.869	5.104	5.289
	FG-X	4.872	5.116	5.330
	FG-nX	4.871	5.114	5.325
1	UD	4.291	4.553	4.787
	FG-V	4.291	4.552	4.782
	FG-O	4.290	4.546	4.763
	FG-X	4.293	4.560	4.811
	FG-nX	4.292	4.559	4.806

(Continued)

Table 9 (continued)

n	CNT distributions	2-1-2	1-1-1	1-2-1
5	UD	3.242	3.448	3.653
	FG-V	3.242	3.445	3.642
	FG-O	3.240	3.437	3.618
	FG-X	3.245	3.458	3.686
	FG-nX	3.244	3.456	3.679
10	UD	3.093	3.247	3.400
	FG-V	3.093	3.244	3.388
	FG-O	3.091	3.236	3.363
	FG-X	3.096	3.258	3.436
	FG-nX	3.095	3.255	3.428

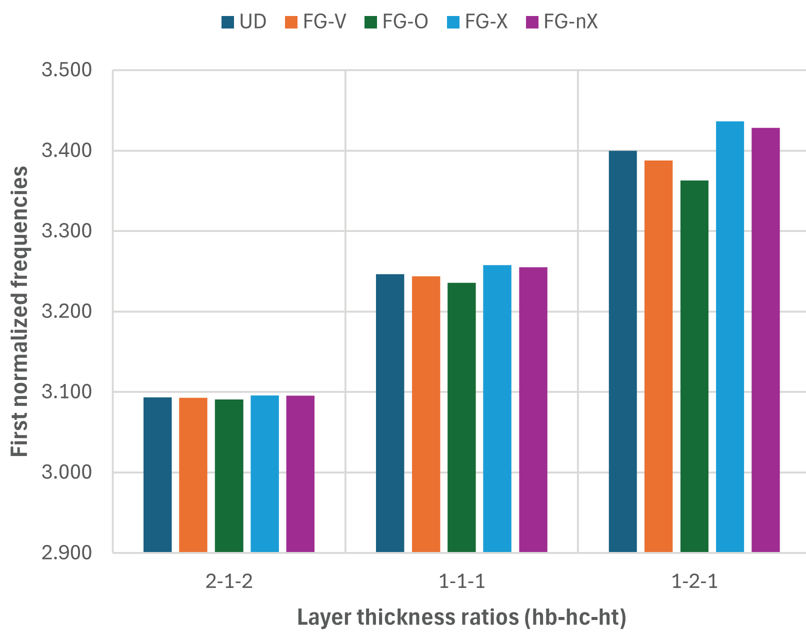

Figure 14: Effect of the layer-thickness ratio on the first normalized frequency of the spherical FGM-FGCNTRC sandwich shell with $h/R_x = 0.008$, $R_x = 1$ m, $R_y = 1$ m, $L_y/R_y = 0.1$, $n = 10$, $L_x = L_y$, $V^*_{CNT} = 0.11$

4.2.3 Hyperbolic-Parabolic FGM-FGCNTRC Sandwich Shells

The geometries of the shells and the normalized frequency and parameter investigations discussed in this section are the same as those in Section 4.2.2 except that we use $R_y = -1$ m in this section. The obtained results for hyperbolic-parabolic FGM-FGCNTRC sandwich shells are presented in Tables 10–12 and in Figs. 15 and 16. Similar to our earlier observations in Section 4.2.2, when more constraints are applied at boundaries, the higher is the frequency of the shell. Also, the higher the thickness-to-radius ratio, the higher the length-to-radius ratio, or the greater the amount of CNTs, the higher the stiffness and frequency of the shell. Here also, FG-X is the best CNT distribution which produces the highest stiffness and frequency of the shell compared to the rest CNT distributions. FG-nX distribution produces a higher stiffness and frequency of the shell than do the UD, FG-V, and FG-O distributions.

Table 10: First six normalized frequencies of hyperbolic-parabolic FGM-FGCNTRC sandwich shells with $R_x = 1$ m, $R_y = -1$ m, $V^*_{CNT} = 0.11$, UD distribution, the layer-thickness ratio 1-2-1, $L_y/R_y = 0.1$, $L_x = L_y$

Boundary	h/R_x	n	Mode					
			1	2	3	4	5	6
SSSS	0.004	0.5	1.573	3.884	3.935	6.183	7.571	7.702
		1	1.410	3.479	3.539	5.549	6.787	6.940
		5	1.068	2.622	2.708	4.204	5.114	5.333
		10	0.997	2.440	2.534	3.920	4.755	4.993
	0.008	0.5	3.067	7.306	7.396	10.260	10.260	11.320
		1	2.753	6.561	6.667	9.451	9.451	10.195
		5	2.086	4.952	5.105	7.289	7.289	7.743
		10	1.945	4.600	4.766	6.632	6.632	7.197
CCCC	0.004	0.5	2.897	5.637	5.705	8.232	9.777	9.946
		1	2.607	5.061	5.140	7.404	8.783	8.976
		5	1.993	3.827	3.941	5.628	6.632	6.903
		10	1.861	3.561	3.684	5.243	6.161	6.452
	0.008	0.5	5.289	9.975	10.077	14.109	16.453	16.706
		1	4.768	8.995	9.116	12.758	14.875	15.152
		5	3.638	6.822	6.997	9.728	11.293	11.656
		10	3.387	6.323	6.510	9.016	10.440	10.822

Table 11: First normalized frequencies of CCCC hyperbolic-parabolic FGM-FGCNTRC sandwich shells with $R_x = 1$ m, $R_y = -1$ m, the layer-thickness ratio 1-2-1, $h/R_x = 0.008$, $L_x = L_y$

L_y/R_y	n	CNT distributions	V^*_{CNT}		
			0.11	0.14	0.17
0.1	1	UD	4.768	4.780	4.794
		FG-V	4.763	4.772	4.783
		FG-O	4.744	4.749	4.757
		FG-X	4.792	4.810	4.830
		FG-nX	4.787	4.803	4.822
	0.5	UD	5.289	5.298	5.310
		FG-V	5.285	5.292	5.301
		FG-O	5.269	5.272	5.278
		FG-X	5.310	5.324	5.341
		FG-nX	5.305	5.319	5.334

(Continued)

Table 11 (continued)

L_y/R_y	n	CNT distributions	V^*_{CNT}		
			0.11	**0.14**	**0.17**
0.2	1	UD	5.595	5.633	5.669
		FG-V	5.583	5.616	5.650
		FG-O	5.569	5.599	5.629
		FG-X	5.622	5.666	5.709
		FG-nX	5.616	5.659	5.701
	0.5	UD	6.184	6.215	6.246
		FG-V	6.173	6.201	6.230
		FG-O	6.161	6.186	6.212
		FG-X	6.206	6.244	6.281
		FG-nX	6.201	6.238	6.274

Table 12: First normalized frequencies of CCCC hyperbolic-parabolic FGM-FGCNTRC sandwich shells with $R_x = 1$ m, $R_y = -1$ m, $h/R_x = 0.008$, $L_y/R_y = 0.1$, $L_x = L_y$, $V^*_{CNT} = 0.11$

n	CNT distributions	2-1-2	1-1-1	1-2-1
0.5	UD	4.843	5.086	5.289
	FG-V	4.843	5.085	5.285
	FG-O	4.842	5.080	5.269
	FG-X	4.845	5.092	5.310
	FG-nX	4.844	5.091	5.305
1	UD	4.265	4.530	4.768
	FG-V	4.265	4.529	4.763
	FG-O	4.264	4.523	4.744
	FG-X	4.267	4.537	4.792
	FG-nX	4.266	4.536	4.787
5	UD	3.221	3.430	3.638
	FG-V	3.221	3.427	3.627
	FG-O	3.219	3.419	3.603
	FG-X	3.224	3.440	3.672
	FG-nX	3.223	3.438	3.664
10	UD	3.075	3.231	3.387
	FG-V	3.074	3.228	3.374
	FG-O	3.073	3.220	3.350
	FG-X	3.078	3.242	3.423
	FG-nX	3.077	3.239	3.415

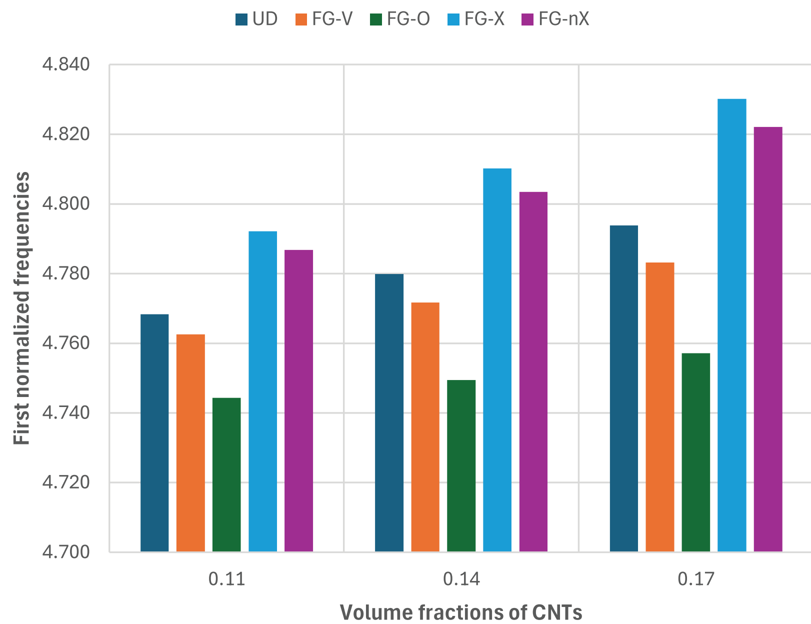

Figure 15: Effect of CNT distribution on the first normalized frequency of the hyperbolic-parabolic FGM-FGCNTRC sandwich shell with $h/R_x = 0.008$, $R_x = 1$ m, $R_y = -1$ m, $L_y/R_y = 0.1$, $n = 1$, $L_x = L_y$ and the layer-thickness ratio 1-2-1

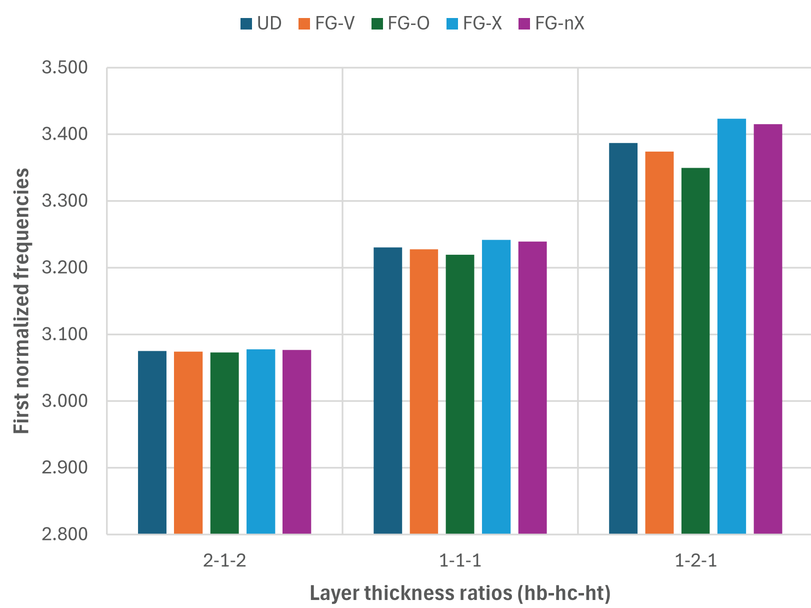

Figure 16: Effect of the layer-thickness ratio on the first normalized frequency of the hyperbolic-parabolic FGM-FGCNTRC sandwich shell with $h/R_x = 0.008$, $R_x = 1$ m, $R_y = -1$ m, $L_y/R_y = 0.1$, $n = 10$, $L_x = L_y$, $V^*_{CNT} = 0.11$

5 Conclusions

In this work, we have presented free vibration analyses of FGM-FGCNTRC sandwich shells utilizing an improved meshfree moving-Kriging method and first-order shear deformation shell theory. The effective material characteristics of both the FGM skin layers and the FGCNTRC core were determined using the rule of mixture. The accuracy of the present formulation was confirmed by solving some problems.

The obtained results agreed well with the reference ones. Some main parameters and factors such as the thickness-to-radius ratio (h/R), the length-to-radius ratio (L/R), the layer-thickness ratio ($h_b - h_c - h_t$), the CNT distribution, the CNT volume fraction V_{CNT}^*, the power-law index n, and the boundary condition were rigorously studied in section Parameter study. The present formulation can be applied to cylindrical, spherical, hyperbolic-parabolic FGM-FGCNTRC sandwich shells and plates. Especially, a nonlinear CNT distribution named FG-nX was first proposed in this work, and an improved meshfree moving-Kriging method was first developed for shell analyses. In addition, many results for FGM-FGCNTRC sandwich shells were first proposed. The following are some of our main conclusions:

- The greater the amount of CNTs, the higher the stiffness and frequency of the shell. FG-X is the best CNT distribution that produces the highest stiffness and frequency of the shell compared to the rest of the CNT distributions. FG-nX (proposed) produces a higher stiffness and frequency of the shell than do the UD, FG-V, and FG-O distributions.
- The thicker the FGCNTRC core, the higher the stiffness and frequency of the shell. It is found that the effect of the CNT distribution on the frequency of the shell is very small for the case where the layer-thickness ratio is 2-1-2, while it is significant for the case where the layer-thickness ratio is 1-2-1. It is recommended to use FGM-FGCNTRC sandwich shells with the layer-thickness ratio 1-2-1 (or shells with thicker FGCNTRC cores) to efficiently exploit the CNT distribution.
- The higher the thickness-to-radius ratio or the length-to-radius ratio, the higher the stiffness and frequency of the shell.

Although the present approach possesses some advantages and some findings for FGM-FGCNTRC sandwich shells have been recommended, some limitations remain to be overcome. These include the following: 1) The present formulation applies to doubly curved shells, but it needs to be improved for analyzing free-form shells; 2) The meshfree MK method should be improved for reducing the computational cost. Overcoming these limitations can be considered as future work. In addition, some possible future research directions include analyses of the transient vibrations, nonlinear vibrations, and nonlinear forced vibrations of FGM-FGCNTRC sandwich shells.

Acknowledgement: None.

Funding Statement: The authors received no specific funding for this study.

Author Contributions: Study conception and design: Tan N. Nguyen, Nuttawit Wattanasakulpong; Literature review and data collection: Tan N. Nguyen, Suppakit Eiadtrong; Analysis and interpretation of literature: Tan N. Nguyen, Suppakit Eiadtrong, Mohamed-Ouejdi Belarbi; Visualization and graphical representation: Tan N. Nguyen, Suppakit Eiadtrong; Draft manuscript preparation: Tan N. Nguyen, Suppakit Eiadtrong; Critical revision of the manuscript: Tan N. Nguyen, Nuttawit Wattanasakulpong, Mohamed-Ouejdi Belarbi. All authors reviewed the results and approved the final version of the manuscript.

Availability of Data and Materials: Data will be made available on request.

Ethics Approval: No applicable.

Conflicts of Interest: The authors declare no conflicts of interest to report regarding the present study.

References

1. Eiadtrong S, Nguyen TN, Wattanasakulpong N. Nonlinear vibration of sandwich beams made of FGM faces and FGP core under multiple moving loads using a quasi-3D theory. Eng Struct. 2024 Oct;316:118575. doi:10.1016/j.engstruct.2024.118575.

2. Reddy JN. Analysis of functionally graded plates. Int J Numer Methods Eng. 2000 Jan;47:663–84. doi:10.1002/(SICI)1097-0207(20000110/30)47:1/3<663::AID-NME787>3.0.CO;2-8.
3. Li Q, Iu VP, Kou KP. Three-dimensional vibration analysis of functionally graded material sandwich plates. J Sound Vib. 2008 Mar;311(1):498–515. doi:10.1016/j.jsv.2007.09.018.
4. Amir M, Lim J, Kim SW, Lee SY. Finite element analysis of natural frequencies of the FGM porous cooling plate with cutouts: a multilayered FGM approach. Results Eng. 2023 Dec;20:101532. doi:10.1016/j.rineng.2023.101532.
5. Bagheri H, Kiani Y, Eslami MR. Free vibration of FGM conical-spherical shells. Thin-Walled Struct. 2021 Mar;160:107387. doi:10.1016/j.tws.2020.107387.
6. Dai L. Book review: carbon nanotubes and related structures-new materials for the twenty-first century. Peter J. F. Harris. ChemPhysChem. 2002 May;3(5):463–4. doi:10.1002/1439-7641(20020517)3:5<463::AID-CPHC463>3.0.CO;2-C/abstract.
7. Lau AKT, Hui D. The revolutionary creation of new advanced materials-carbon nanotube composites. Compos Part B Eng. 2002 Jun;33(4):263–77. doi:10.1016/s1359-8368(02)00012-4.
8. Thostenson ET, Li C, Chou TW. Nanocomposites in context. Compos Sci Technol. 2005 Mar;65(3):491–516. doi:10.1016/j.compscitech.2004.11.003.
9. Iijima S. Helical microtubules of graphitic carbon. Nature. 1991;354(6348):56–8. doi:10.1038/354056a0.
10. Civalek O, Dastjerdi S, Akgöz B. Buckling and free vibrations of CNT-reinforced cross-ply laminated composite plates. Mech Based Des Struct Mach. 2022 Apr;50:1914–31. doi:10.1080/15397734.2020.1766494.
11. Yee K, Ghayesh MH, Ng CT. Coupled five-parameter dynamics of Mindlin and third-order shear deformable FG graphene-platelets reinforced viscoelastic plates with geometric and material imperfections. Eng Struct. 2023 Dec;297(3–5):116944. doi:10.1016/j.engstruct.2023.116944.
12. Pagani A, Augello R, Carrera E. A high-order shell finite element for the large deformation analysis of soft material structures. Int J Numerical Meth Eng, 125(7):e7417. doi:10.1002/nme.7417.
13. Zhang Q, Li S, Zhang AM, Peng Y, Yan J. A peridynamic Reissner-Mindlin shell theory. Int J Numerical Meth Eng. 2021 Jan;122:122–47. doi:10.1002/nme.6527.
14. Eroğlu M, Koç MA, Esen I. Thermomechanical free vibration buckling of FG graphene-reinforced doubly-curved sandwich shells. Adv Eng Softw. 2025 Apr;202:103875. doi:10.1016/j.advengsoft.2025.103875.
15. Lakhdar Z, Chorfi SM, Belalia SA, Khedher KM, Alluqmani AE, Tounsi A, et al. Free vibration and bending analysis of porous bi-directional FGM sandwich shell using a TSDT p-version finite element method. Acta Mech. 2024 Jun;235(6):3657–86. doi:10.1007/s00707-024-03909-y.
16. Zhou L, Yang H, Ma L, Zhang S, Li X, Ren S, et al. On the static analysis of inhomogeneous magneto-electro-elastic plates in thermal environment via element-free Galerkin method. Eng Anal Bound Elem. 2022 Jan;134(1):539–52. doi:10.1016/j.enganabound.2021.11.002.
17. Rabczuk T, Areias PMA, Belytschko T. A meshfree thin shell method for non-linear dynamic fracture. Int J Numer Methods Eng. 2007 Oct;72(5):524–48. doi:10.1002/nme.2013.
18. Nguyen TN, Thai CH, Nguyen-Xuan H, Lee J. Geometrically nonlinear analysis of functionally graded material plates using an improved moving Kriging meshfree method based on a refined plate theory. Compos Struct. 2018 Jun;193(1):268–80. doi:10.1016/j.compstruct.2018.03.036.
19. Sadamoto S, Ozdemir M, Tanaka S, Taniguchi K, Yu TT, Bui TQ. An effective meshfree reproducing kernel method for buckling analysis of cylindrical shells with and without cutouts. Comput Mech. 2017;59(6):919–32. doi:10.1007/s00466-017-1384-5..
20. Nguyen TN, Wattanasakulpong N, Nguyen NP, Fakharian P, Eiadtrong S. Isogeometric analysis of functionally graded triply periodic minimal surface shells. Mech Adv Mater Struct. 2025. doi:10.1080/15376494.2024.2423278.
21. Nguyen TN, Thai CH, Luu AT, Nguyen-Xuan H, Lee J. NURBS-based postbuckling analysis of functionally graded carbon nanotube-reinforced composite shells. Comput Methods Appl Mech Eng. 2019 Apr;347(6348):983–1003. doi:10.1016/j.cma.2019.01.011.
22. Nguyen TN, Hien TD, Nguyen-Thoi T, Lee J. A unified adaptive approach for membrane structures: form finding and large deflection isogeometric analysis. Comput Methods Appl Mech Eng. 2020 Sep;369:113239. doi:10.1016/j.cma.2020.113239.

23. Nguyen SN, Nguyen-Thoi T, Trinh MC, Ho-Nguyen-Tan T, Han JW. Smoothed finite element approach for viscoelastic behaviors of general shell structures. Thin-Walled Struct. 2022 Jul;176(1–4):109323. doi:10.1016/j.tws.2022.109323.
24. Vaghefi R. Analysis of thermo-elastoplastic bending behavior of FG skew sandwich plates on elastic foundation using an enhanced meshless radial basis reproducing kernel particle approach. Arch Appl Mech. 2024;94(11):3195–227. doi:10.1007/s00419-024-02666-7.
25. Najafi M, Dehghan M, Šarler B, Kosec G, Mavrič B. Divergence-free meshless local Petrov-Galerkin method for Stokes flow. Eng Comput. 2022 Dec;38(6):5359–77. doi:10.1007/s00366-022-01621-w.
26. Tomar S, Singh M, Vajravelu K, Ramos H. Simplifying the variational iteration method: a new approach to obtain the Lagrange multiplier. Math Comput Simul. 2023 Feb;204(7–8):640–4. doi:10.1016/j.matcom.2022.09.003.
27. Gao H, Wei G. A meshless solution of nonlinear elastoplastic problems based on the RRKPM. Results Phys. 2021 Dec;31:104986. doi:10.1016/j.rinp.2021.104986.
28. Krongauz Y, Belytschko T. Enforcement of essential boundary conditions in meshless approximations using finite elements. Comput Methods Appl Mech Eng. 1996 Apr;131(1):133–45. doi:10.1016/0045-7825(95)00954-x.
29. Gu L. Moving kriging interpolation and element-free Galerkin method. Int J Numerical Meth Eng. 2003 Jan;56:1–11. doi:10.1002/nme.553.
30. Tongsuk P, Kanok-Nukulchai W. Further investigation of element-free galerkin method using moving kriging interpolation. Int J Comput Methods. 2004 Sep;01(02):345–65. doi:10.1142/S0219876204000162.
31. Bui TQ, Nguyen TN, Nguyen-Dang H. A moving Kriging interpolation-based meshless method for numerical simulation of Kirchhoff plate problems. Int J Numer Meth Eng. 2009 Mar;77:1371–95. doi:10.1002/nme.2462.
32. Sayakoummane V, Kanok-Nukulchai W. A meshless analysis of shells based on moving kriging interpolation. Int J Comput Meth. 2007 Dec;04:543–65. doi:10.1142/S0219876207000935.
33. Bui TQ, Nguyen MN, Zhang C, Pham DAK. An efficient meshfree method for analysis of two-dimensional piezoelectric structures. Smart Mater Struct. 2011 May;20(6):065016. doi:10.1088/0964-1726/20/6/065016.
34. Bui TQ, Nguyen MN, Zhang C. An efficient meshfree method for vibration analysis of laminated composite plates. Comput Mech. 2011 Aug;48(2):175–93. doi:10.1007/s00466-011-0591-8.
35. Nguyen TN, Thai CH, Nguyen-Xuan H. A novel computational approach for functionally graded isotropic and sandwich plate structures based on a rotation-free meshfree method. Thin-Walled Struct. 2016 Oct;107(6–8):473–88. doi:10.1016/j.tws.2016.06.011.
36. Thai CH, Nguyen TN, Rabczuk T, Nguyen-Xuan H. An improved moving Kriging meshfree method for plate analysis using a refined plate theory. Comput Struct. 2016 Nov;176(1):34–49. doi:10.1016/j.compstruc.2016.07.009.
37. Thai CH, Do VNV, Nguyen-Xuan H. An improved moving Kriging-based meshfree method for static, dynamic and buckling analyses of functionally graded isotropic and sandwich plates. Eng Anal Bound Elem. 2016 Mar;64(12):122–36. doi:10.1016/j.enganabound.2015.12.003.
38. Pandey S, Pradyumna S. Transient stress analysis of sandwich plate and shell panels with functionally graded material core under thermal shock. J Therm Stresses. 2018 May;41:543–67. doi:10.1080/01495739.2017.1422999.
39. Pandey S, Pradyumna S. A finite element formulation for thermally induced vibrations of functionally graded material sandwich plates and shell panels. Compos Struct. 2017 Jan;160(2):877–86. doi:10.1016/j.compstruct.2016.10.040.
40. Fu T, Wu X, Xiao Z, Chen Z. Study on dynamic instability characteristics of functionally graded material sandwich conical shells with arbitrary boundary conditions. Mech Syst Signal Process. 2021 Apr;151(5):107438. doi:10.1016/j.ymssp.2020.107438.
41. Dung DV, Hoa LK, Thuyet BT, Nga NT. Buckling analysis of functionally graded material (FGM) sandwich truncated conical shells reinforced by FGM stiffeners filled inside by elastic foundations. Appl Math Mech. 2016 Jul;37(7):879–902. doi:10.1007/s10483-016-2097-9.
42. Moita JS, Araújo AL, Mota Soares CM, Mota Soares CA. Vibration analysis of functionally graded material sandwich structures with passive damping. Compos Struct. 2018 Jan;183:407–15. doi:10.1016/j.compstruct.2017.04.045.

43. Dung DV, Nga NT, Hoa LK. Nonlinear stability of functionally graded material (FGM) sandwich cylindrical shells reinforced by FGM stiffeners in thermal environment. Appl Math Mech. 2017 May;38(5):647–70. doi:10.1007/s10483-017-2198-9.
44. Fu T, Wu X, Xiao Z, Chen Z, Li J. Vibro-acoustic characteristics of eccentrically stiffened functionally graded material sandwich cylindrical shell under external mean fluid. Appl Math Model. 2021 Mar;91(2):214–31. doi:10.1016/j.apm.2020.09.061.
45. Mehar K, Panda SK, Mahapatra TR. Nonlinear frequency responses of functionally graded carbon nanotube-reinforced sandwich curved panel under uniform temperature field. Int J Appl Mech. 2018 Apr;10(3):1850028. doi:10.1142/S175882511850028X.
46. Tung HV, Trang LTN. Nonlinear stability of advanced sandwich cylindrical shells comprising porous functionally graded material and carbon nanotube reinforced composite layers under elevated temperature. Appl Math Mech. 2021 Sep;42(9):1327–48. doi:10.1007/s10483-021-2771-6.
47. Ninh DG, Ha NH, Long NT, Tan NC, Tien ND, Dao DV. Thermal vibrations of complex-generatrix shells made of sandwich CNTRC sheets on both sides and open/closed cellular functionally graded porous core. Thin-Walled Struct. 2023;182(7):110161. doi:10.1016/j.tws.2022.110161.
48. Duc ND, Seung-Eock K, Khoa ND, Chan DQ. Nonlinear buckling and post-buckling analysis of shear deformable stiffened truncated conical sandwich shells with functionally graded face sheets and a functionally graded porous core. J Sandw Struct Mater. 2021 Oct;23:2700–35. doi:10.1177/1099636220906821.
49. Wang YQ, Xing WC, Wang J, Chai Q. Theoretical and experimental studies on vibration characteristics of bolted joint multi-plate structures. Int J Mech Sci. 2023 Aug;252:108348. doi:10.1016/j.ijmecsci.2023.108348.
50. Zhu P, Lei ZX, Liew KM. Static and free vibration analyses of carbon nanotube-reinforced composite plates using finite element method with first order shear deformation plate theory. Compos Struct. 2012 Mar;94(4):1450–60. doi:10.1016/j.compstruct.2011.11.010.
51. Li X, Gao H, Scrivens WA, Fei D, Xu X, Sutton MA, et al. Reinforcing mechanisms of single-walled carbon nanotube-reinforced polymer composites. J Nanosci Nanotechnol. 2007 Jul;7(7):2309–17.
52. Esawi AMK, Farag MM. Carbon nanotube reinforced composites: potential and current challenges. Mater Des. 2007 Jan;28(9):2394–401. doi:10.1016/j.matdes.2006.09.022.
53. Seidel GD, Lagoudas DC. Micromechanical analysis of the effective elastic properties of carbon nanotube reinforced composites. Mech Mater. 2006 Aug;38(8):884–907. doi:10.1016/j.mechmat.2005.06.029.
54. Anumandla V, Gibson RF. A comprehensive closed form micromechanics model for estimating the elastic modulus of nanotube-reinforced composites. Compos Part A Appl Sci Manuf. 2006 Dec;37(12):2178–85. doi:10.1016/j.compositesa.2005.09.016.
55. Sobhani Aragh B, Nasrollah Barati AH, Hedayati H. Eshelby-Mori-Tanaka approach for vibrational behavior of continuously graded carbon nanotube-reinforced cylindrical panels. Compos Part B Eng. 2012 Jun;43(4):1943–54. doi:10.1016/j.compositesb.2012.01.004.
56. Wang J, Pyrz R. Prediction of the overall moduli of layered silicate-reinforced nanocomposites—part I: basic theory and formulas. Compos Sci Technol. 2004 Jun;64(7):925–34. doi:10.1016/s0266-3538(03)00024-1.
57. Shen HS, Zhang CL. Thermal buckling and postbuckling behavior of functionally graded carbon nanotube-reinforced composite plates. Mater Des. 2010 Aug;31(7):3403–11. doi:10.1016/j.matdes.2010.01.048.
58. Shen HS. Nonlinear bending of functionally graded carbon nanotube-reinforced composite plates in thermal environments. Compos Struct. 2009;91(1):9–19. doi:10.1016/j.compstruct.2009.04.026.
59. Reddy JN. Mechanics of laminated composite plates and shells: theory and analysis. Boca Raton, FL, USA: CRC Press; 2003.
60. Nguyen TN, Lee S, Nguyen-Xuan H, Lee J. A novel analysis-prediction approach for geometrically nonlinear problems using group method of data handling. Comput Methods Appl Mech Eng. 2019 Sep;354(1):506–26. doi:10.1016/j.cma.2019.05.052.
61. Zhang LW, Lei ZX, Liew KM, Yu JL. Static and dynamic of carbon nanotube reinforced functionally graded cylindrical panels. Compos Struct. 2014 May;111:205–12. doi:10.1016/j.compstruct.2013.12.035.
62. Liew KM, Lim CW. Vibration of doubly-curved shallow shells. Acta Mech. 1996 Mar;114(1):95–119. doi:10.1007/BF01170398.